Characterization of Magnetic Hyperthermia in Magnetic Nanoparticles

8

Eva Natividad and Irene Andreu

Contents

1   Definition of the Topic

Certain magnetic nanoparticles are able to generate heat through magnetic moment reversal processes under the action of an adequate alternating magnetic field. This ability, together with biocompatibility and nanosize of the particles, makes them promising materials for biomedical applications. Among the potential applications is magnetic hyperthermia, an oncological therapy expected to battle malignant tumors with minimal side effects by using localized heating. The success of the therapy requires, among others, accurate quantification of the released heat leading to the

E. Natividad (✉) • I. Andreu
Instituto de Ciencia de Materiales de Aragón (ICMA), CSIC - Universidad de Zaragoza, Zaragoza, Spain
e-mail: evanat@unizar.es; iandreub@sfu.ca

prediction of the temperature increase in and around the treatment area. This chapter is devoted to the recent advances in the determination of this heating ability.

2   Overview

The heating ability of magnetic nanoparticles is quantified by means of the Specific Absorption Rate (SAR), also referred to as Specific Loss Power (SLP), which accounts for the heat power released per unit mass of magnetic material. While magnetic hyperthermia is nowadays an approved anticancer therapy, there exist neither standardized experimental setups nor protocols to determine the heating ability of magnetic nanoparticles under the action of alternating magnetic fields. A wide variety of special-purpose mostly noncommercial setups are currently used to determine SAR either by magnetic or calorimetric approaches. These methods and setups are revised in this chapter, together with their inaccuracies and their possible minimization.

On the other hand, the SAR value of a magnetic nanoparticle increases with the amplitude, H_0, and frequency, f, of the applied alternating magnetic field, since more electromagnetic energy is invested in magnetic reversal processes. But these parameters are limited to human-tolerated values in magnetic hyperthermia. The prediction of SAR as a function of H_0 and f in this range is challenging and strongly dependent on the nature, geometry, and size of the nanoparticles, which govern their magnetic state. In this chapter, both experimental and theoretical results on this subject are displayed and discussed. Also, particular examples highlighting the interest of measuring SAR as a function of the temperature are provided. Eventually, the unavoidable interparticle magnetic interactions, arising from the concentration and acquired arrangement of nanoparticles and responsible for the nonnegligible modification of SAR values, are tackled.

3   Introduction

Cancer is, by statistics from 2010, the second most common cause of death across the European Union and the United States, as reported by Eurostat [1] and the National Center for Health Statistics [2]. Classical anticancer therapies, i.e., surgery, chemo- and radiotherapy, face harmful side effects due to the lack of selectivity of the cytotoxic agents or cannot be applied upon some tumor locations and conditions. Therefore, major efforts are devoted to boosting the effectiveness of these therapies or to developing new ones in order to increase the survival rate and improve the quality of life of cancer patients under treatment.

Clinical hyperthermia is currently the fourth most important therapeutic approach for cancer treatment. It is based on the mild heating (between 42 °C and 50 °C) of the area under treatment for a desired amount of time, inducing a heat-shock response in the metabolism of the cells that depends on the thermal dose, the target tissue, and other physiological parameters [3]. A localized heating is desired in the case of small

and/or well defined tumors. In particular, magnetic hyperthermia, also known as magnetic fluid hyperthermia, is a promising local hyperthermia therapy, in which magnetic nanoparticles (MNPs) are responsible for supplying heat to the tissue using electromagnetic to thermal energy conversion. If the MNPs are dispersed only within the tumor region, the heat generated will produce a localized temperature increase during the time of application of an externally generated alternating magnetic field, AMF.

Experimental investigations on magnetic hyperthermia started in 1957 with the work of Gilchrist et al. [4]. Although there has been ongoing research since then, the last 20 years have been the most productive for this research field, nourished by the optimization of MNP synthetic procedures, a better understanding of cell-level biology and development of more accurate characterization methods, high-quality AMF applicators, and realistic thermal simulations. In 2011, the European Union approved magnetic hyperthermia for treatment of glioblastoma multiforme after the promising results obtained in the phase II clinical trial carried out by the company MagForce (Berlin, Germany) [5], and up-to-date, magnetic hyperthermia is offered to the public as a complement to radiotherapy.

The NanoTherm$^{®}$ therapy is currently performed in several steps. First, the ferrofluid containing the MNPs is injected into the tumor. Afterwards, the acquired MNP distribution is studied by computed tomography. Using this information, the therapy is planned by means of special-purpose software that uses the so-called bioheat transfer equation to simulate the spatial and temporal temperature distribution in and around the tumor area. Once the adequate H_0 value and duration are established, the therapy is finally applied. The achieved temperatures are monitored by thermometers previously installed using catheters.

From this process, it is easy to infer that the success of the therapy is partially based on the capability of simulating as precisely as possible the acquired maximum temperatures, in order to achieve a therapeutic effect where required, while preserving the healthy tissue. Simulations require quantification of several parameters: geometrical, physiological or thermal, both of the tissues and of the MNPs. In particular, accurate SAR values are crucial for feeding the simulations, as well as for tailoring the MNP characteristics for optimal heating ability. This heating ability depends on the AMF parameters [6] and on the individual characteristics of the MNPs [7–10], but also on the concentration and geometrical arrangement acquired by the MNPs in the tissue [11]. All these factors must be taken into account when evaluating SAR.

4   Experimental and Instrumental Methodology

At present, many research groups are involved worldwide in the characterization of magnetic nanoparticle hyperthermia. Two main approaches are used to measure SAR: magnetic detection or calorimetric determination, the latter being much more widespread. Although some specific-purpose setups are commercially available [12], most groups have chosen to build their own setups or to use other

experimental facilities leading to the determination of SAR data such as commercial magnetometers. In this section, the currently used methods and setups for SAR determination are described.

4.1   Alternating Magnetic Field Generation

Regardless of the technique used for SAR measurement, an AMF generation means is required, since the magnetic hyperthermia phenomenon occurs when magnetic nanoparticles turn the AMF electromagnetic energy into heat.

The more used AMF source is the copper coil [12–15], with a variable number of turns (2 to 70). Also, the AMF can be created within the gap of ferrite-core electromagnets [16–19], as well as inside superconducting coils immersed in a proper cryogenic liquid [20, 21].

4.2   Magnetic Detection

One way of determining SAR is measuring the magnetic response of a sample subjected to an applied AMF. The SAR can be then calculated using theoretical expressions that relate such response with the released heat power. In particular, a MNP subjected to an external AMF takes electromagnetic energy from the field to reverse its magnetization, which in turn results in a release of heat [22]. This magnetic response can be determined by different types of magnetic measurements, based on the quantification, through different sensors, of the current induced in a gradiometric inductive coil due to the changes over time in the magnetic flux density produced by the sample [23].

4.2.1   Hysteresis Loops

When an AMF is applied to a ferro/ferrimagnetic material, the magnetization, M, vs. applied field, H, describes a hysteresis loop due to the nonlinearity and delay of M with respect to H. The area entrapped within the cycle accounts for the heat dissipated per cycle, and SAR can be calculated from quantification of this area as [24],

$$\text{SAR} = \frac{f\mu_0}{\rho_{MNP}} \oint M(H)dH \tag{8.1}$$

where $\mu_0 = 4\pi \times 10^{-7}$ T $\cdot$ m/A is the permeability of free space, ρ_{MNP} is the density of the magnetic material, and M and H are expressed in SI units (A/m). According to Eq. 8.1, SAR can be computed by calculating the value of the closed integral of the experimental $M(H)$ curve and taking into account the AMF frequency.

Hysteresis loops can be obtained using commercial magnetometers such as, for example, vibrating sample magnetometers (VSM) [25] or superconducting quantum

interference device (SQUID) magnetometers [26], as well as homemade gradiometric coils [27].

4.2.2 Ac Susceptibility

When a MNP is subjected to an AMF whose amplitude, H_0, is small enough as to fulfill the requirements of the linear response theory (LRT), then the value of its magnetization is linearly proportional to H_0. This means that its magnetic susceptibility, χ, depends on the AMF frequency, but not on H_0. Considering χ in its complex form, $\chi = \chi' - i\chi''$, where χ' and χ'' are the in-phase and out-of-phase components of the magnetic susceptibility, respectively, and assuming a sinusoidal AMF [24], Eq. 8.1 changes into,

$$\text{SAR} = \frac{\pi\mu_0}{\rho_{MNP}} f H_0^2 \chi''$$ (8.2)

which relates χ'' and the AMF parameters with the released heat power.

According to Ref. [28] and considering an isolated MNP, the LRT is only valid when,

$$H_0 < \frac{k_B T}{\mu_0 M_S V_M}$$ (8.3)

where M_s and V_M are, respectively, the saturation magnetization and the magnetic volume of the MNP in SI units, k_B is the Boltzmann constant and T is the temperature. Equation 8.3 indicates that the LRT is only valid for small H_0 values and that the maximum H_0 value for LRT validity decreases with increasing V_M.

Some of the most widespread commercial devices for magnetic measurements may work as ac-susceptometers, which allow performing χ'' high-sensitivity measurements as a function of temperature, T, f, and H_0.

4.3 Calorimetric Detection

The other approach to determine SAR is measuring the temperature increase of a sample subjected to an AMF and calculating SAR afterwards, this time using thermal models that describe the thermal conditions in which the experiment takes place. In a general thermal model for SAR measurement, a sample of volume V, specific heat capacity c, thermal conductivity k, and density ρ contains a mass of magnetic material m_{MNP}. This sample is initially at the same temperature than its environment, T_0. At $t = t_0$ the AMF is switched on and the MNPs generate heat, so that the sample can be considered a material with heat sources inside. The total released power P is SAR·m_{MNP}. If we assume that the heat sources (MNPs) are homogeneously distributed across the sample, then heat power per volume unit is P/V. The heat generated by the MNPs is *diffused* across the sample, and the heat flux arriving to the sample limits is continuously transferred to the sample

environment (container, insulator, air. . .) by conduction, convection and radiation. These phenomena originate a spatial and temporal temperature distribution within the sample, governed by,

$$\rho \cdot c \cdot \frac{\partial T\left(\vec{r},t\right)}{\partial t} = k \cdot \nabla^2 T\left(\vec{r},t\right) + \frac{P}{V} \tag{8.4}$$

The analytical solution of this differential equation in partial derivatives is complex, making difficult the establishment of a theoretical expression relating T and P.

This thermal model is appreciably simplified if, in an idealization of the system, the temperature gradients across the sample are neglected, so that the sample temperature is considered always homogeneous. This assumption gives reasonable estimations when the internal (inside the sample) thermal relaxation time is about ten times lower than the external (sample to its environment) one [29]. Within this approximation, the temporal evolution of the sample temperature can be inferred from the power balance between the sample and its environment. This balance obviously depends on the thermal conditions of the experimental setup.
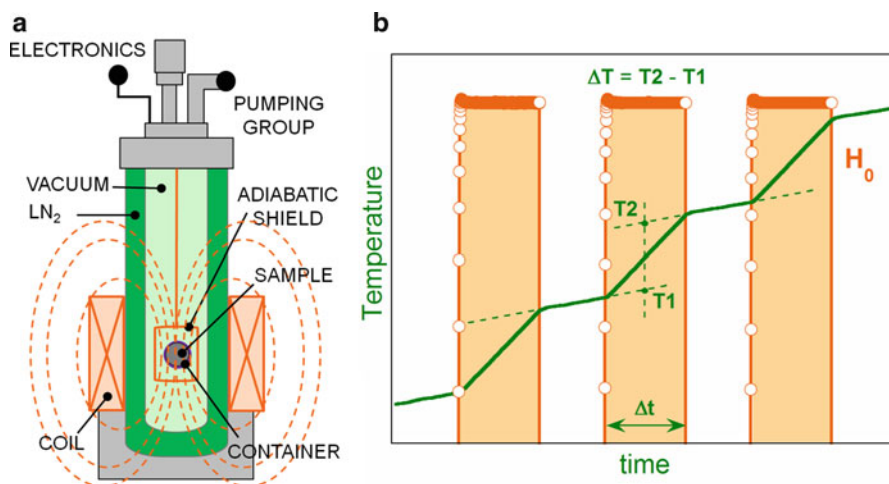
4.3.1   Adiabatic Conditions

In ideal adiabatic conditions, no heat transfer occurs between the sample and its environment. To achieve such measuring conditions, the temperature of the sample environment must be continuously kept equal to that of the sample, which results in minimization of thermal losses and, as a consequence, in the investment of all the released heat in the sample heating. Given that thermal relaxation to the environment does not occur, it is reasonable to use power balances to describe the system is these conditions. This balance can be written as,

$$P = C \cdot \frac{dT(t)}{dt} \tag{8.5}$$

where C is the heat capacity of the sample. Assuming that P and C do not vary with T, which can be achieved using small heating intervals, the integration of Eq. 8.5 derives a simple analytical expression,

$$\Delta T = \frac{P}{C}\Delta t \rightarrow SAR = \frac{\Delta T}{\Delta t}\frac{C}{m_{MNP}} \tag{8.6}$$

relating linearly SAR and T, where ΔT is the temperature increment undergone by the sample upon application of a heating pulse of duration Δt. At present and to our knowledge, there is only one experimental setup capable of measuring SAR in adiabatic conditions [13]. A scheme of this setup is shown in Fig. 8.1a. The AMF is provided by a 30-turn coil placed outside the glass vessels (vacuum and liquid nitrogen), so that the eventual heating at high field amplitudes does not interfere in the adiabatic control. Adiabatic conditions are achieved by holding the sample (and its container) using poorly conductive means (e.g., thin threads) in the vacuum

Fig. 8.1 SAR determination in adiabatic conditions: (**a**) scheme of the setup described in Ref. [13]; (**b**) calculation of ΔT by the pulsed heating method

environment, to avoid conduction and convection. Sample and container are surrounded by a nonmetallic radiation shield with heating means (resistive-alloy thin film heater) whose temperature must be continuously controlled to the same temperature of the sample, so that thermal radiation losses to the shield cannot occur due to absence of temperature differences between them. Holding threads and temperature sensor wires (thermocouples) are thermalized in the radiation shield, to reduce thermal gradients.

In real systems, achieving strict adiabatic conditions is impossible, and a very weak heat transfer between the sample and its environment is always present. To account for this interchange, the magnitude ΔT in Eq. 8.6 is calculated by the *pulse heating method*, used in traditional adiabatic calorimetry. Once in adiabatic conditions, the sample temperature is registered before, during, and after application of a heating pulse of duration Δt. An example of a *T*-vs.-*t* characteristic is shown in Fig. 8.1b, in which the linear drifts due to the presence of very small heat losses (or gains) are indicative of acceptable adiabatic conditions. Corrections of these small thermal losses are performed by linear fitting the temperature drifts in equilibrium and subtracting the extrapolations of both drift rates toward the midpoint of Δt, as indicated in Fig. 8.1b. This method then calculates SAR using *stationary* states of the sample.

4.3.2 Isoperibol Conditions

In isoperibol conditions, the temperature of the sample varies, but the temperature of *its* environment is always constant. Assuming that the internal (inside the sample) thermal relaxation time is about ten times lower than the external (sample to its environment), the power balance that can be used in this case is
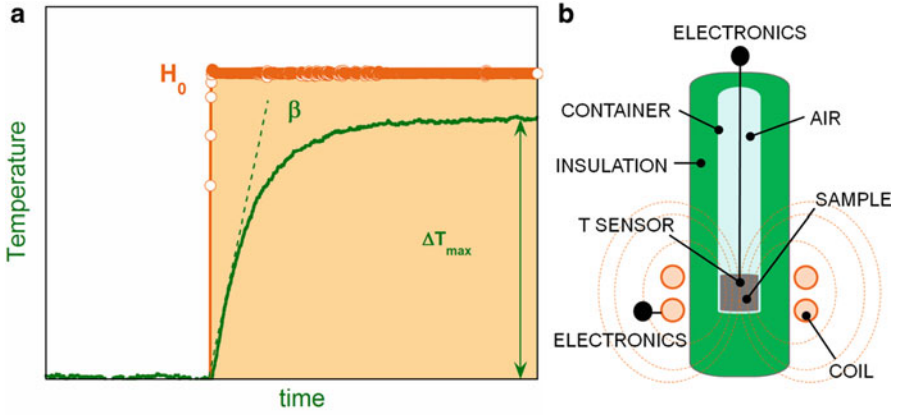
Fig. 8.2 SAR determination in isoperibol conditions: (**a**) *T*-vs-*t* characteristic and calculation of β; (**b**) scheme of a typical setup

$$P = C \cdot \frac{dT(t)}{dt} + L \cdot [T(t) - T_0] \tag{8.7}$$

where L(W/K) is a coefficient accounting for losses. This balance indicates that the released heat is partly invested in the sample heating and partly transferred to the environment. Assuming that the losses between the sample and its environment are linear with T, (i.e., that L is constant) and that P and C do not vary with T, the integration of Eq. 8.7 derives an analytical expression that relates SAR and T by means of the thermal losses to the environment,

$$T(t) = T_0 + \Delta T_{\max} \left[1 - e^{-\frac{t}{\tau_i}} \right] \tag{8.8}$$

where $\Delta T_{\max} = P/L$, and $\tau_i = C/L$. In the stationary state, the heat generated and lost become equal, and the sample temperature remains constant at a value $T_{\max} = T_0 + \Delta T_{\max}$.

To simplify the calculations and avoid the use of L, SAR determination in isoperibol conditions is often performed using the *initial-slope method*, which is based on the additional assumption of that the heat losses are negligible during a certain time interval at the beginning of the heating process. The derivative of Eq. 8.8 at the onset of heating then is

$$\left. \frac{dT}{dt} \right|_{t \to 0} = \frac{\Delta T_{\max}}{\tau} \left(e^{-\frac{t}{\tau}} \right) \Big|_{t \to 0} = \frac{P}{C} \to \text{SAR} = \frac{C}{m_{MNP}} \cdot \left. \frac{dT}{dt} \right|_{t \to 0} = \frac{C}{m_{MNP}} \cdot \beta \tag{8.9}$$

where the initial slope, β, is calculated within the time interval in which heat losses are negligible (see Fig. 8.2a). This method then calculates SAR in *transient* states of the sample temperature.

Currently, the most part of the research groups working on MFH have adopted this initial-slope method [14, 16, 18–21, 30–61]. A scheme of one of the used setups is shown in Fig. 8.2b. In it, the sample is placed into a circular two-turn coil inside a test tube, and temperature variations are measured by means of a fiber optic. Similar setups have been built in several laboratories and some are also commercially available. Samples are placed in different containers: glass or plastic test tubes, plastic or glass vials, glass capillaries, centrifuge or microcentrifuge tubes, plastic capsules and also especial-purpose holders in polypropylene or Teflon, glass flasks with vacuum shield, etc. The volume of the container is either partially or fully occupied by the sample. The sample container is often partially or fully thermally linked with room air by different poorly heat-conducting means, such as vacuum vessels, 2-walled glass vessels with air flow, polymeric foams, asbestos, polypropylene, or Teflon. The temperature of the sample is registered by different contact or noncontact sensors, usually fiber optic probes but also thermistors, thermocouples, organic liquid thermometers, pyrometers, and IR cameras. T vs. t data within a certain initial time interval, which varies from several tens of seconds to several minutes, are used to calculate the initial slope. This can be done by differentiation of a fit (linear [37, 41, 62], polynomial [30, 46]) or by direct calculation of $\Delta T/\Delta t$ [18, 35, 40, 51]. Some authors use numerical differentiation, and given that the initial T-vs.-t trend is not strictly linear and the slope is nonconstant, they use maximum slopes [60, 63] or constant slopes [45] to determine SAR. In summary, there is a large variety of setups and measuring conditions.

4.3.3   In Vivo Conditions

When MNP heating takes place in vivo, it is not possible to neglect temperature gradients across the sample (the body tissue). Accordingly, temporal power balances cannot be used to describe the temperature evolution of the treated area.

The reached temperature does not only depend on the heat generated by the MNPs, but also on the geometry of the target region, the MNPs spatial distribution, the thermal properties of the tissues, and other factors such as blood convection. Equation 8.4 must be then adapted to biological systems, giving rise to the so-called bioheat transfer equation [64, 65].

The simplest useful equation deriving physically sound results for magnetic hyperthermia is known as the Pennes heat transfer equation [64]. It describes the spatial and temporal evolution of the temperature in biological systems neglecting blood convection and assuming that the heat transfer between blood and surrounding tissues mainly occurs in the capillary bed. It then considers heat losses just by conduction and blood perfusion. The Pennes bioheat equation reads,

$$\rho c \frac{\partial T}{\partial t} = \nabla \cdot k \nabla T - W_b \rho_b c_b (T - T_b) + \frac{P_m}{V} + \frac{P}{V} \qquad (8.10)$$

where the magnitudes without subscripts are relative to the tissue, W_b, ρ_b, c_b, and T_b are the perfusion constant, mass density, specific heat, and temperature of the blood, respectively, and P_m is the metabolic heat power generation.

Pennes equation can be solved analytically for simple cases. However, numerical methods such as finite element, finite difference, or Monte Carlo methods are currently used [66] to solve this equation for realistic tumor geometries in practical applications.

At this point, it seems rather evident that in vivo conditions are not adequate to provide accurate SAR values. On the contrary, SAR values obtained with other accurate techniques should be used to feed the bioheat transfer equation ($P = \text{SAR} \cdot m_{MNP}$) and calculate the temperature distribution in and around the target region as function of the AMF characteristics and the exposure time. This would help in providing the right therapeutic temperature where required, while avoiding overheating and damaging of the surrounding healthy tissue [67].

5 Key Research Findings

5.1 Inaccuracies of Available Experimental Methods

One of the concerning consequences of the use of a large variety of setups and measuring conditions for SAR determination is the always presumed and sometimes demonstrated existence of important inaccuracies of the obtained data. In this section, the sources of uncertainties, as well as their possible minimization, will be discussed.

5.1.1 Alternating Magnetic Field Generation

The first source of data inaccuracy is the characteristics of the generated AMF. Three main requirements should be expected from a suitable AMF source:

- It must have a sample space with a constant and well-known H_0.
- It must minimize the thermal interchange with the sample.
- It must generate H_0 and f values in the biological range of field application.

Given that the heating generated by MNPs under an AMF is strongly dependent on H_0, it is thus very important that the whole sample volume is subjected to the same AMF, and that the heating output is assigned to the correct H_0 value. Then the first requirement should be ensured by special-purpose careful designs of the AMF source and corroborated by simulations [13, 34, 68, 69]. For example, for assuring a constant H_0 in coils, it is important that their height is much larger than the sample space, since H_0 decreases towards the coil limits [70].

The second requirement is aimed at avoiding any temperature increase of the sample due to an eventual heating of the AMF source. This can be achieved either by thermal isolation of the sample or by refrigeration of the coil. In the first case, vacuum or an effective insulator layer can be used. In the second, the coil may be cooled by means of a circulating liquid (water, air, nonane) or directly be immersed in a cryogenic liquid.

Eventually, the values of H_0 and f that can be safely used at in vivo applications are restricted to a certain range due to unwanted responses of the organism. Measuring SAR out of this range necessarily implies the use of extrapolations but, as explained later in the chapter, the SAR values obtained with a given H_0 and f values cannot be easily extrapolated to other H_0 and f values. For this reason, measurements in the correct H_0 and f range are highly preferable.

5.1.2 Magnetic Methods

Let us first discuss the calculation of SAR from hysteresis loops as explained in Sect. 4.2.1. VSM or SQUID magnetometers are commercial equipment present in many laboratories involved with magnetism. These setups allow recording hysteresis loops up to sufficiently high H_0 values, and therefore, they should be suitable to calculate SAR. However, these commercial setups measure magnetization in presence of a magnetic field varying at very low frequency, much smaller than those used for MFH. Going back to Eq. 8.1, we find at first glance that SAR depends linearly with frequency, so that extrapolations to the right f do not seem a source of error in SAR determination. But as it will be explained in next sections, the area of the loop, represented by the closed integral in Eq. 8.1, may also depend on f. In these cases, measuring hysteresis cycles with the wrong f value may drive to a misleading SAR determination.

Ideally, the area of the hysteresis loops should be determined applying AMFs with the typical parameters for MFH, to avoid uncertainties derived from frequency effects. Up to the authors' knowledge, there is no commercial equipment committed to the measurement of $M(H)$ cycles in the biological range of AMF application, due to the difficulty in measuring magnetization at frequencies in the range of the kilohertz [25]. Nevertheless, such homemade devices have been developed by some research groups [17, 27, 37, 69, 71–73]. It is worth highlighting the devices in Refs. [27, 69] and [74] which measure temperature while recording $M(t)$ and $H(t)$ during AMF application at typical f and H_0 for MFH.

A similar problem is encountered when SAR is calculated from χ'' measurements. The typical AMF parameters involved in commercial setups (e.g., for MPMS and PPMS devices from Quantum Design Inc., respectively, ($f = 10$ Hz–10 kHz, $H_0 \leq 1.2$ kA/m or $f = 0.1$ Hz–1 kHz, $H_0 \leq 0.2$ kA/m) are outside the MFH typical range. However, high-frequency ac-susceptometers have been built [27, 38, 39, 75–78], with frequencies up to 1 MHz, more suitable for MFH applications. One of them is currently commercially available [75]. They use $H_0 \leq 0.5$ kA/m, with an exception [77], where H_0 reaches 3.2 kA/m. Even in these setups, extrapolations are generally needed to obtain SAR values at the H_0 for MFH applications, with the inherent inaccuracies that this implies. It must be pointed that the system described in Ref. [27] determines simultaneously χ'' and the hysteresis loop area from the temporal evolution of H and M. The SAR obtained with both magnetic methods displays a good agreement.

In addition to typical experimental considerations for general magnetic measurements (e.g., diamagnetic corrections for sample holders and dispersive media), the T at which the measurement is performed must be monitored. Since the studied

MNPs are designed for heating applications, some temperature increase is expected during measurements, due to heat generated by the MNPs. As SAR depends on T, it is important to control T during measurements, or at least assign each SAR value with the T during each measuring process.

5.1.3 Calorimetric Methods

The pulse heating method in adiabatic conditions is considered the unique "absolute" and the most accurate and direct method for the determination of heat capacities [79, 80] and, by analogy, of SAR. Indeed, for heat capacity determination, a heat pulse of duration Δt is provided to the sample by a calibrated heater, and the heat capacity of the sample is obtained and, in SAR determination, the heat capacity of the sample is known, and the heat provided by MNPs upon application of an AMF pulse is calculated. However, the main drawback for the applicability of this method is the availability of an adequate setup providing adiabatic conditions.

The accuracy of the pulse heating method in adiabatic conditions for SAR determination was experimentally evaluated with the setup described in Sect. 4.3.1 by measuring the induction heating power of a copper cylinder [13]. The experimental value was compared to the theoretical one and calculated using the analytical expression for the heating power dissipated due to Foucault currents by a metallic semi-infinite cylinder in a uniform axial AMF. Both values were found to differ only in 3 %.

The initial-slope method in isoperibol conditions should also provide accurate results if the requirements assumed in Sect. 4.3.2 were fulfilled. These are:

- The internal (inside the sample) thermal relaxation time is about ten times lower than the external (sample to its environment).
- The temperature of the *sample* environment is always constant.
- The losses between the sample and its environment are linear with T.

These requirements highly depend on thermal and geometrical parameters of the sample and its environment and vary for each experimental setup. For the first requirement, the most suitable case of application would involve a highly conductive sample with a weak thermal link to its environment. This would allow assuming a homogeneous temperature distribution inside the sample, a very important fact for the initial-slope determination, which takes place in transient conditions. The second would imply temperature control means, and the third, study and adequacy of the sample-environment thermal link.

The main problem with this technique is that the widespread utilization of the initial-slope method has driven to an incorrect systematic use of Eq. 8.9 as a quasi-exact definition of SAR, and the requirements exposed above are seldom checked. As a consequence, obtained results may present from small to large *unknown* uncertainties, and for this reason, data so-obtained must be handled with care, and considered in many cases an estimate.

The inaccuracies arising from this method have been studied in some cases. For example in Ref. [81], the same setup, sample, and temperature sensor used in the

determination of the accuracy of the pulse heating method in adiabatic conditions was utilized to carry out measurements without temperature control. It was confirmed that the use of the initial-slope method could underestimate the theoretical SAR by 21 %.

Also in Ref. [81], the effect of the SAR calculation method, as well as insulating conditions, temperature sensors, and sample-sensor contacts, was studied. Taking the accurate SAR value obtained by the pulse heating method as a reference, the uncertainties of the initial-slope method were determined. Using as temperature sensor a glued thermocouple, SAR underestimations between 2 and 34 % were obtained under different isolation conditions. Higher underestimations of 48–50 % were obtained using a pyrometer or a fiber-optics thermometer through the container wall, with polystyrene foam as insulator. Finally, with polystyrene foam as insulator, and the fiber-optics thermometer inside the ferrofluid, the SAR was either overestimated (5 %, using a $\Delta t = 40$ s for linear regression) or underestimated (12 %, using a $\Delta t = 120$ s for linear regression).

More recently, the sources of errors in measuring SAR using the initial-slope method were studied by numerical simulations [70, 82]. The temperature distribution across a ferrofluid volume was studied using parameters typical of experimental setups working under isoperibol conditions. It was found that the sample volume required to obtain a reduced error must be relatively high, e.g., 2.5 ml or more for a power density of 3.8 W/cm^3, and that the inaccuracies depend on the generated heat power, the specific heat of the sample, and the thermal losses of the system. Among the studied cases, the best results were obtained when the temperature sensor was placed at the position where the sample temperature was maximal. This position varied depending on the experimental conditions. Eventually, short interval times (of the order of several seconds) provide in general less error.

In sum, the initial-slope method in isoperibol conditions would certainly improve accuracy through (i) the development of a more accurate thermal model describing more precisely a reference experimental setup and (ii) the modification of the currently used setups to mimic that reference one.

5.2   Effects of the Alternating Magnetic Field Amplitude and Frequency

One of the present challenges of magnetic hyperthermia is reaching therapeutic temperatures with minimal MNP doses [83]. In other words, MNPs able to generate high heat power are continuously pursued. However, the SAR values one can encounter across the scientific literature vary several orders of magnitude. Then, some questions arise. Are those differences reliable? Or are MNPs displaying appealing SAR values of up to 10^4 W/g always more suitable for magnetic hyperthermia than those showing overlookable SAR values of 1 W/g? To answer these questions properly, the relationship between the MNP properties and the parameters (H_0, f) of the applied AMF must be taken into consideration.

Table 8.1 Critical sizes for the SPM/FM-SD and FM-SD/MD transitions in common magnetic materials at room temperature [84]

Material	Size (nm)	
	SPM/FM-SD	FM-SD/MD
CoFe$_2$O$_4$	9.4	100
Fe$_2$O$_3$	31	91
Fe$_3$O$_4$	25	83
FeCo	15	51
FePt	2.8	54
CoPt	2.9	56
Ni	29	85
Co	9.7	80
Fe	8.0	50

5.2.1 Magnetic States of a MNP

Let us consider a single, immobilized MNP. The main parameters that influence its heating ability are: the applied magnetic field, the temperature, the magnetization, and the magnetic anisotropy constant, K, the last two being MNP properties that depend on temperature, composition, shape, and size. For a given temperature (e.g., room temperature), a given MNP composition (e.g., magnetite, Fe$_3$O$_4$) and a given shape (e.g., spherical), then M_S and K are governed by the MNP size. Large MNPs (>83 nm for Fe$_3$O$_4$ [84]) show a ferro/ferrimagnetic multidomain (FM-MD) magnetic structure. In each domain, all the magnetic moments are coupled together, but depending on the applied magnetic field, the magnetization of different domains may or may not be parallel. As MNP size is reduced, an intermediate vortex state [85] leads to a single-domain (FM-SD) structure, in which the magnetic moments of the whole MNP are coupled together. And as the MNP size decreases below a certain value ($\cong$25 nm for Fe$_3$O$_4$ [84]), the magnetization reversal processes are not only governed by H, but also by thermal fluctuations. The MNP is still single-domain, but enters the superparamagnetic (SPM-SD) state in which, due to size reduction, the magnetostatic energy of the particle becomes low enough that it is comparable to its thermal energy, allowing thermally induced magnetization relaxations, which are characterized by the Néel relaxation time, τ_N. Other materials different from Fe$_3$O$_4$ require other MNP sizes to enter the FM-SD or the SPM-SD state at a fixed temperature (see Table 8.1). The size for the onset of the SPM-SD state mainly depends on K, while that for the FM-SD state depends also on M and on the stiffness of the exchange interaction between magnetic moments [85, 86]. But in general, the sizes of FM-MD nanoparticles are too high to be interesting for magnetic hyperthermia.

5.2.2 Effects of f and H_0 in the SAR of SD Nanoparticles Near the SPM/FM Transition

Due to the thermally induced magnetization reversal processes in superparamagnets, the $M(H)$ loops recorded for one of these MNPs under slowly varying AMFs have a sigmoidal shape in which no hysteresis is observed. This does not imply that such

MNPs are unable to undergo hysteresis losses when subjected to an AMF, since dynamic $M(H)$ loops at adequate frequencies may show hysteresis. According to the Rosensweig model of superparamagnetism [24], the out-of-phase ac-susceptibility, indicative of dissipative processes, can be expressed as,

$$\chi'' = \chi_0 \cdot \frac{2\pi f \tau}{1 + (2\pi f \tau)^2} \tag{8.11}$$

where χ_0 is the static susceptibility and τ is the magnetic moment relaxation time, which stands for the Néel relaxation time in case of an immobilized MNP. The simplified expression for this time is,

$$\tau \equiv \tau_N = \tau_0 \exp\left(\frac{KV_M}{k_B T}\right) = \tau_0 \exp\left(\frac{E_{b0}}{k_B T}\right) \tag{8.12}$$

where τ_0 is the attempt time, $\tau_0 = 10^8$–10^{10} s and E_{b0} is the barrier energy for magnetization reversal, created by the anisotropy energy of the MNPs.

It is easily deduced from Eq. 8.11 that χ'' has a maximum at $2\pi f \tau = 1$, whose value is $\chi_0/2$. This maximum occurs at the SPM/FM transition. In particular, the T at which this transition takes place is called the blocking temperature (T_B), which delimits the FM ($T < T_B$) and the SPM ($T > T_B$) behavior. In order to locate T_B at therapeutic temperatures and optimize heat dissipation, the frequency of the AMF must be tuned with respect to the MNP properties, or vice versa. For a given f, MNP composition, and shape, the MNP size can be tuned as

$$V_M^{Opt} = \frac{k_B T_B}{K} \ln \frac{1}{2\pi f \tau_0} \tag{8.13}$$

where V_M^{Opt} corresponds to the MNP volume that has its SPM/FM transition at T_B. The optimal conditions are much more sensitive to the size of the MNPs than to the f of the AMF. For example, using $T_B = 300$ K, $K = 32$ kJ/m^3 and $\tau_0 = 10^{-9}$ s and assuming spherical MNPs, Eq. 8.13 is fulfilled at 100 kHz with a particle diameter of 12.2 nm, while for 400 kHz the optimal diameter is 11.4 nm: a fourfold increase of the frequency leads to only a 6 % decrease of the optimal particle diameter.

As seen in Eq. 8.2, χ'' and SAR are linearly related in the LRT approach. In this framework, χ_0 can be approximated to the initial susceptibility of the Langevin equation [24],

$$\chi_0 \cong \frac{\mu_0 M_S^2 V_M}{3 k_B T} \tag{8.14}$$

and SAR can be expressed as,

$$\text{SAR} = \frac{\pi \mu_0}{\rho_{MNP}} \cdot \frac{\mu_0 M_S^2 V_M}{3 k_B T} \cdot H_0^2 \cdot f \frac{2\pi f \tau}{1 + (2\pi f \tau)^2} \tag{8.15}$$

This theoretical development highlights the dependency of SAR on f and H_0 within the LRT limits. Although χ'' presents a maximum at $2\pi f \tau = 1$, SAR presents a nonlinear growing trend with f, due to the increasing number of the AMF cycles described per time unit (see Fig. 8.3a). Also, SAR increases with H_0^2. The difference in using H_0 values of, for example, 4 kA/m instead of 1 kA/m is obtaining a SAR value 16 times higher. So, the effect of both magnitudes, but especially H_0, is notorious, and it is then imperative to provide the H_0 and f value with each SAR datum. Eventually, within the LRT limits, the SAR value obtained with a given H_0 value can be easily extrapolated to other H_0 values, but the same statement is not true for f, where a more complicated dependence is found.

The limits of LRT (see Eq. 8.3) are not, however, wide enough to enclose the whole biological range of AMF application. For example, the size of a magnetite nanoparticle ($M_S = 446$ kA/m) subjected to an AMF of $H_0 = 5$ kA/m and $f = 100$ kHz at 300 K should be under 14 nm to fulfill the LRT. The use of higher H_0 values would require smaller MNPs for the LRT to be valid, and vice versa. Out of these limits, Eqs. 8.11, 8.12, and 8.13 are still valid, but not Eqs. 8.14 and 8.15, and the relationship between SAR and the AMF parameters is not straightforward.

To our knowledge, no analytical expressions of the dependence of SAR on H_0 or f are available out of the LRT. However, numerical simulations aiming to calculate dynamic hysteresis loop areas can be used to infer some trends. With respect to the influence of H_0, for example, numerical calculations based on a two-level approximation [28] predict that the LRT model overestimates the hysteresis area of SPM nanoparticles right above the LRT limits, indicating that the SAR would be proportional to H_0 to a power lower than 2. Further results arising from this model will be tackled in Sect. 5.2.3. Another interesting result of numerical simulations [87] is that, at large enough H_0 values, increasing H_0 implies shifting the dissipation maximum to higher frequencies. This is due to the fact that in that strong nonlinear regime, the barrier energy for magnetization reversal gets appreciably reduced by H_0, so that τ depends not only on the materials properties, but also on H_0. This would make SAR dependence on H_0 stronger or weaker than predicted by the LRT, at higher or lower frequencies, respectively, than that corresponding to the condition of the maximum of Eq. 8.11. Also, it has been found [88, 89] that an increase in H_0 also entails a widening of the SAR maxima as a function of the MNP size, this implying that in this situation, even MNP assemblies with a certain size distribution will present a good performance, due to the less restricted tuning condition between f and V_M.

Let us now qualitative contrast these theoretical findings with recent experimental data. For this purpose, SAR/f (and not SAR) is studied in order to highlight just the influence of H_0 and f on the hysteresis area, and not the linear dependence on f resulting of increasing the number of the AMF cycles. Figure 8.3b and c illustrate the effects of the $f\tau$ product on SAR. In Fig. 8.3b, experimental SAR/f values are depicted as a function of H_0. These data include iron oxide SPM-SD nanoparticles and some FM-SD nanoparticles next to the SMP/FM limit. For each data series, H_0 and f are constant, but the MNP size varies (see Table 8.2). This size variation induces a great change in τ, thus making SAR/f vary several orders of magnitude, according to Eq. 8.15. Figure 8.3c displays the variation of SAR/f on f for SPM-SD
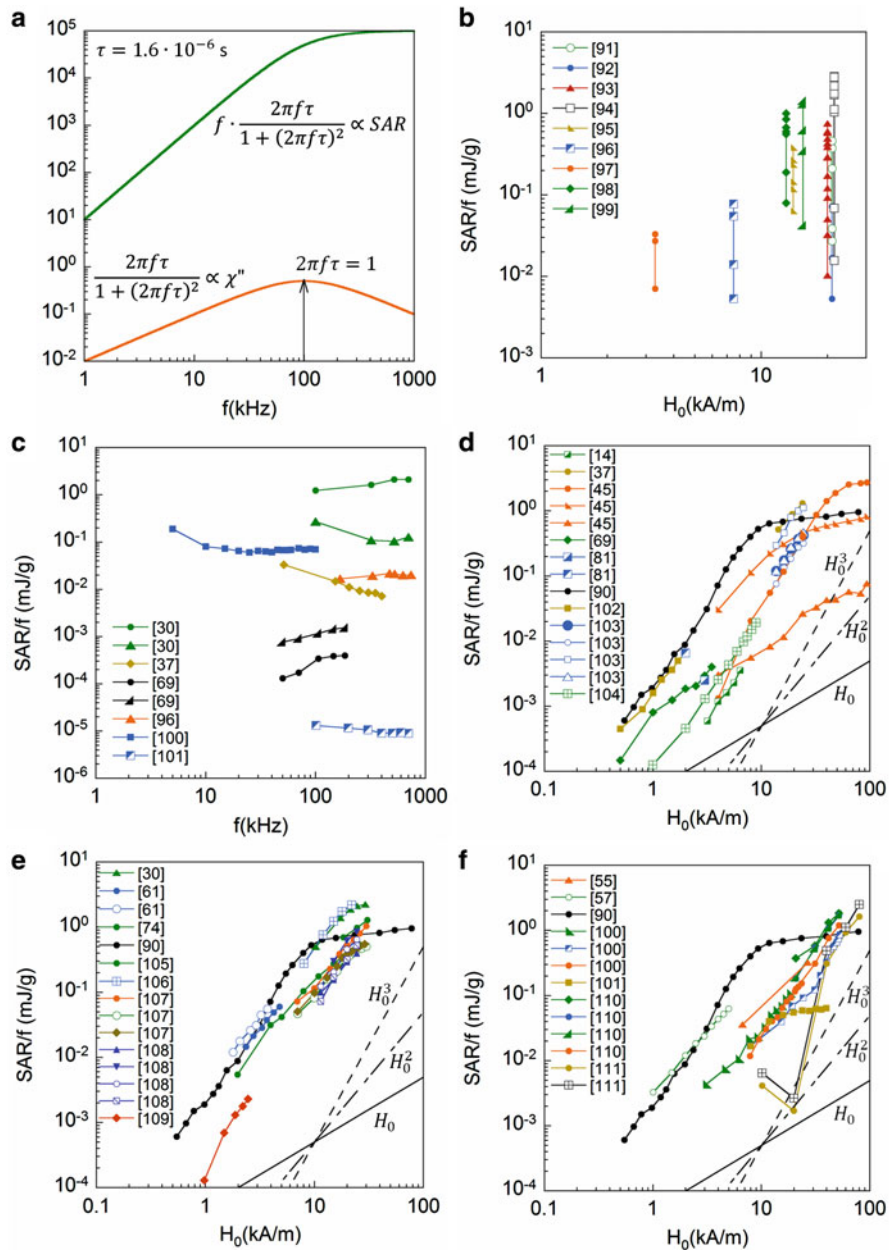
Fig. 8.3 SAR of SD MNPs near the SPM/FM transition: (**a**) theoretical dependency on f of χ'' and SAR (LRT limit); (**b**) effect of MNP size at constant H_0, f; (**c**) effect of f at constant H_0, size; (**d, e**, and **f**) effect of H_0 at constant f and size for iron oxide (**d, e**) and non-iron-oxide (**f**) MNPs. Curves aiding to identify H_0, H_0^2 and H_0^3 dependencies are also included in figures **d, e** and **f**

Table 8.2 Experimental details of the data collected in Fig, 8.3

Ref.	material	size (nm)	medium	f (kHz)	H_0 (kA/m)
[14]	Fe_3O_4	20	Water	236	3.2–6.4
[30]	Multicore Fe_2O_3	10.3–28.8	Water	520	21
	Multicore Fe_2O_3	24.0	Water	100–700	25
	Micromod BNF-Starch (Fe_3O_4)	44	Water	520	25
	Multicore Fe_2O_3	24.0	Water	520	10–30
[37]	Fe_3O_4	25	Water	50–400	4.7 14.3–24.0
[45]	Micromod BNF-Starch (Fe_3O_4)	44	Water	141	4–94
	Nanomag-D-Spio (Fe_3O_4)	10–12	Water	141	4–94
	Feridex (Fe_3O_4+ Fe_2O_3)	4–10	Water	141	4–94
[55]	$MgFe_2O_3$	20	Water	265	6.7–26.7
[57]	Co	12.0	Water	500	1–5
[61]	Fe_3O_4	11.0	Water/normal saline	200	2–4.3
[69]	Fe_2O_3	10.9	Mineral oil	50–185 100	1/2 0.5–3.5
[74]	Fe_2O_3	13.5	Acid water	394	2–28
[81]	Endorem (iron oxide, multicore)	150	Water	109	3
	Chemicell Fluid MAG (Fe_3O_4)	~15	Water	109	2
[90]	Magnetosomes(Fe_3O_4+ Fe_2O_3)	30	Agarose gel	0.05	0.1–100
[91]	Fe_3O_4	4–35	Water	168	21
[92]	Fe_3O_4	6–18	Water	700	21
[93]	Fe_3O_4 + Fe_2O_3	5–18	Hexane	765	21
[94]	Fe_2O_3	6–55	Water	700	21.5
[95]	Fe_3O_4	9–18	Water	373	14
[96]	Fe_2O_3	6–14 13	Water Water	522.7 116–739	7.5 4
[97]	Fe_3O_4	8.8/13.5	Water/normal saline	200	2.3
[98]	Fe_3O_4	6–23	Toluene	100	13
[99]	Fe_3O_4	7–76	Water	500	15.5
[100]	Fe	5.5	Mesitylene	2–300	15.4 0–52.5
[101]	$Co_{1.5}Ti_{0.5}Fe_1O_4$	12	Powder	100–700 50	3.9 4–39.5
[102]	Fe_3O_4	9.8		750	0–2
[103]	iron oxide	5–14	Water + PBS	400	13.5–24.5
[104]	Fe_3O_4	10.3	Transformer oil	1500	1–9
[105]	Fe_3O_4	10	Water/cell culture med.	250	18.5–30.6

(*continued*)

Table 8.2 (continued)

Ref.	material	size (nm)	medium	f (kHz)	H_0 (kA/m)
[106]	Fe_2O_3+ Fe_3O_4	19	Water	320	8–22
[107]	Fe_2O_3	12	Laponite clay	150	7–30
[108]	Fe_2O_3	8.0/12.0	n-Hexane	765	11.5–24.7
		6.5/9.0	n-Hexane	765	11.5–24.7
[109]	Fe_3O_4	9	Water	13,560	1–7
[110]	$MnFe_2O_3$	5.3/7.2	Water	266	20.7–51.6
		10.5/12.1	Water	266	20.7–51.6
[111]	FeCo	5.9	Water + albumin	120	10–80
	FeNi	4.6	Water + albumin	120	10–80

nanoparticles with various compositions (see Table 8.2). For each data series, H_0 and V_M are constant. It is observed that some of these series show the maximum that delimits the FM (above the maximum) and the SPM (below the maximum) regime for each particular MNP size. All these results stand out the relevant and nonlinear dependence of SAR on the AMF frequency in the SPM-SD regime, indicating that extrapolating SAR data according to a linear dependence on f is not always correct.

Figure 8.3 also collects recent experimental evidence of the effect of H_0 on SAR/f data in the SPM-SD regime or in the FM-SD regime next to the SMP/FM limit. As a comparison reference between values, the same series of SAR/f data [90] is included in some graphics. It corresponds to FM-SD nanoparticles and will be discussed in next section. In addition, in order to estimate the exponent of the H_0^n dependence of SAR, trends proportional to H_0, H_0^2, and H_0^3 are also included.

Figure 8.3d and e shows data corresponding to iron-oxide materials. It is first observed that when H_0 is sufficiently high so that major loops are described, SAR becomes independent of H_0 due to saturation of the magnetization. For minor loops, different dependencies are found, but most data can be fitted to H_0^n curves with n ranging between 1.8 and 2.5. They thus present deviations from the LRT according to the numerical simulations referred above. Figure 8.3f, which displays data of materials other than iron oxides (see Table 8.2), derives similar results. In addition, Fig. 8.3e, which shows the most recent data, highlights the evolution in the optimization of SAR in iron-oxide materials, since SAR values are obtained at relatively low H_0 values. Comparatively, non-iron-oxide MNPs (Fig. 8.3f) require greater AMF amplitudes to produce similar heating.

In sum, most of the available experimental data of SD nanoparticles near the SPM/FM transition do not follow the LRT, due to the mostly high H_0 values used. This reinforces the abovementioned requirement of the adequacy of measuring SAR with H_0 and f values in the biological range of field application, since no analytical expressions are available out of the LRT. For example, measuring SAR at high H_0 values (e.g., 20 kA/m) and extrapolating it to lower value (e.g., 5 kA/m) using a H_0^2 law would either underestimate or overestimate this value, if the real dependency is, respectively, weaker or stronger on H_0. Eventually, Fig. 8.3 points out that the same MNP can display a wide range of SAR values and that outstanding SAR values are often indicative of high H_0 values.

5.2.3 Effects of *f* and H_0 in the SAR of FM Nanoparticles

A MNP in the FM state does not undergo thermally induced magnetization relaxations, but its magnetization describes a hysteresis loop upon application of a slowly varying AMF cycle, i.e., a quasi-static hysteresis loop, whose coercive field (H_C) value accounts for the FM hardness or softness of the MNP.

The Stoner–Wohlfarth model [112, 113] is a simple analytical model that describes the main features of the quasi-static hysteresis of FM-SD nanoparticles considering each particle as a macrospin, assuming uniaxial anisotropy and neglecting thermal fluctuations. According to this model, the maximum energy per volume unit that a MNP can dissipate during a hysteresis loop is

$$E_{\text{hyst, max}} = 4 \cdot \mu_0 \cdot M_S \cdot H_K = 8 \cdot K \quad (8.16)$$

where $H_K = 2 \cdot K/\mu_0 \cdot M_S$ is the anisotropy field (in SI units). This is the area of an ideal major square loop, in which the magnetic moment of the MNP is parallel to H and then $H_C = H_K$. For other orientations between M and K, $H_C < H_K$ and E_{hyst} decreases. In particular, for a randomly oriented nanoparticle assembly, this area is [114],

$$E_{\text{hyst, max}} \cong 2 \cdot \mu_0 \cdot M_S \cdot H_C \quad (8.17)$$

which in terms of SAR becomes

$$(\text{SAR}/f)_{\text{max}} \cong 2 \cdot \mu_0 \cdot M_S \cdot H_C/\rho_{MNP} \quad (8.18)$$

According to these results, it seems straightforward to consider that for an improved heating ability, FM MNPs must present a large anisotropy constant leading to a high H_C value. This can be achieved, for example, controlling the size, since it is well known that H_C increases as the size of a MNP grows from the SPM/FM-SD to the FM-SD/MD transition size, showing a maximum at the latter and decreasing for larger sizes [85]. However, the Stoner–Wohlfarth model also predicts that a minimum critical field is necessary for the magnetization to get oriented with the applied field. The existence of this critical field, related to the anisotropy constant, implies that lower H_0 values will not produce appreciable losses.

Some early data [90, 115] will be here used as a starting point to illustrate the above consideration. Figure 8.4 collects SAR/*f* values of four samples determined as a function of H_0 through quasi-static minor loops. These samples have H_C and M_S values ranging between 2.6 and 32.8 kA/m and 333 and 450 kA/m, respectively. Data [90], the series already included in Fig. 8.3, correspond to the heating ability of bacterial magnetosomes, MNPs fabricated by magnetotactic bacteria and widely considered as very good performing material for magnetic hyperthermia. Figure 8.4 reveals the following phenomena:

• SAR/*f* may vary several orders of magnitude when H_0 ranges from 1 to 100 kA/m, being the SAR/*f* values obtained at a certain H_0 value hardly extrapolable to other H_0 values if the particular SAR/*f* (H_0) trend is unknown.
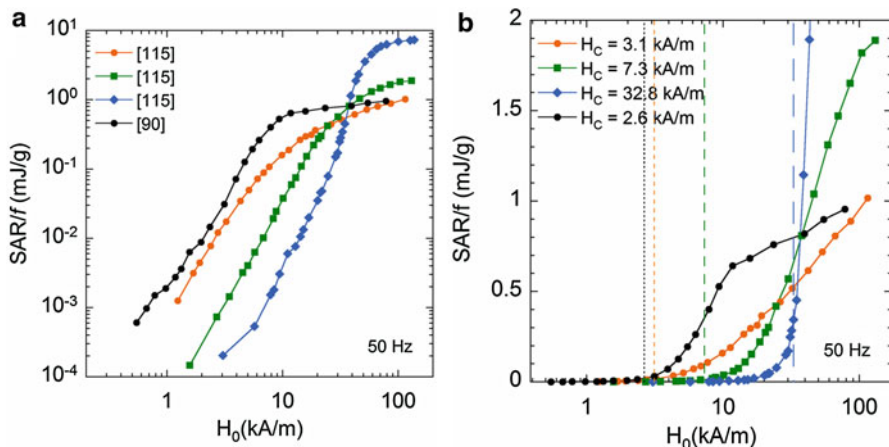
Fig. 8.4 Dependence on H_0 of the SAR of iron oxide FM-SD nanoparticles (Adapted from Ref. [90, 115]). Both figures show the same data, but Figure: (**a**) highlights the low-H_0 dependency; (**b**) displays the significant SAR/f increase at $H_0 \cong H_C$. Each H_C is marked with a vertical line of the same color than the symbols

- For $H_0 >> H_C$ and when major hysteresis loops are considered, the higher H_C is, the larger SAR/f is. It is observed that SAR/f first increases with H_0 and then reaches a plateau that corresponds to the description of a major loop, due to the saturation of M at this H_0 value. The SAR/f value in this plateau is larger/smaller for the sample with higher/lower H_C.
- For $H_0 < H_C$, the higher H_C is, the smaller SAR/f is. It is easily inferred from Fig. 8.4b that SAR/f increases significantly only when $H_0 > H_C$.

These phenomena are essentially in accordance with the Stoner–Wohlfarth model, although some aspects are not. For example, nonzero SAR/f data are obtained for H_0 values below the critical field of the Stoner–Wohlfarth model, showing H_0^n laws. This highlights the limitations of this model to describe precisely the SAR/f dependency on H_0. Another limitation in this model is the absence of dynamic parameters, thus neglecting frequency effects in SAR/f, i.e., in the area of dynamic hysteresis loops.

Some more recent works have looked deeper into the influence of H_0 and f in FM-SD nanoparticles through analytical models and numerical calculations [28, 89, 114, 116–118]. For example, Usov et al. [118] obtained, through a modification of the Stoner–Wohlfarth model, an analytical expression to account for the variation of H_C with V_M, f, and T. For an oriented MNP assembly,

$$H_C = H_K \cdot \left(1 - \kappa^{1/2}\right) \text{ with } \kappa = \frac{k_B T}{K V_M} \cdot \ln\left(\frac{k_B T}{K V_M} \cdot \frac{H_k t_m}{\tau_0 \Delta H}\right) \tag{8.19}$$

where t_m is the time elapsed between the fields H and $H + \Delta H$ during the hysteresis loop. Equation 8.19 is valid for $\kappa < 0.7$ and when major loops are described [28]. According to it, H_C increases when t_m decreases, i.e., when f grows.
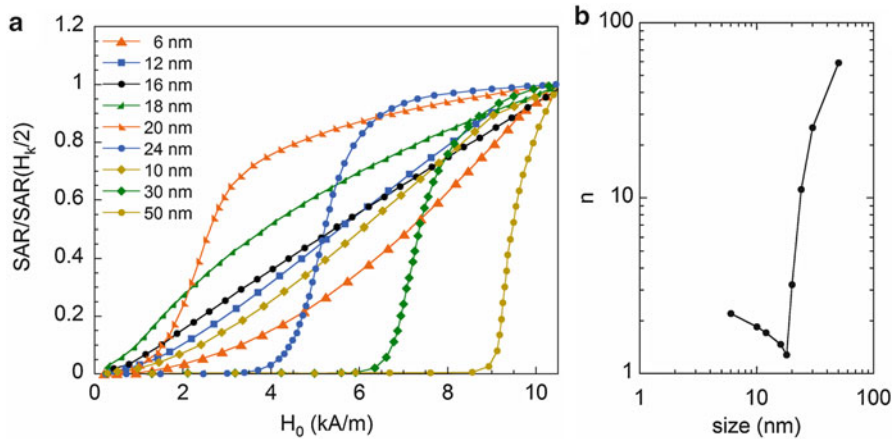
Fig. 8.5 (**a**) H_0 dependence of the ratio SAR/SAR($H_K/2$) for SD nanoparticles of different sizes and $K = 13$ kJ/m^3, $M_S = 10^3$ kA/m, $f = 100$ kHz, $T = 300$ K and $\tau_0 = 5 \times 10^{-11}$ s (Adapted from Ref. [28]). (**b**) n values obtained from fitting to a $H_0{}^n$ law the data of the medium-H_0 range of Fig. 8.5a

The influence of H_0 in SAR/f has been inferred from numerical calculations of dynamic hysteresis loops, obtained using a two-level approximation [28]. This model allows calculating major and minor hysteresis loops for both SPM and FM-SD particles. Figure 8.5a illustrates the H_0 dependence of the ratio SAR/SAR ($H_K/2$) obtained within this model for $K = 13$ kJ/m^3, $M_S = 10^3$ kA/m, $f = 100$ kHz, $T = 300$ K, and $\tau_0 = 5 \times 10^{-11}$ s. With these data, $H_K = 20.69$ kA/m, and the volume that maximize χ'' at 100 kHz according to the LRT (i.e., that defines the SPM/FM transition) is $V_M = 3.30 \times 10^{-24}$ m^3, which corresponds to a particle size of 18.5 nm. For this particle, the LRT is just fulfilled for $H_0 < 1$ kA/m.

It is observed that the curves present three main ranges: (i) low-H_0, in which SAR increases slowly, (ii) medium-H_0, in which SAR experiments a more or less sharp increase, (iii) high-H_0, in which SAR saturates. Figure 8.5b displays the n values obtained from fitting the data of the medium-H_0 range to an $H_0{}^n$ law, showing that this exponent trend undergoes an inflexion point at the SPM/FM transition. Also, it is found that $1.3 < n < 2.2$ in the SPM regime, which is in accordance with the experimental results of Sect. 5.2.2. It becomes obvious that H_0 is a highly influent parameter and that SAR data obtained at a particular H_0 value are not easily extrapolable to other H_0 values, considering in addition that all trends in Fig. 8.5 will be quantitatively different for other material properties. The above results also highlight the suitability of nanoparticles with sizes next to the SPM/FM limit (18–20 nm) for low-H_0 applications and that of larger particles for higher fields.

Eventually, Fig. 8.6 collects recent experimental SAR/f data of FM-SD nanoparticles as a function of f and of H_0. Sample details are collected in Table 8.3. Figure 8.6a displays constant or decreasing SAR/f curves with increasing f, according to the H_C shift predicted by Eq. 8.19, except for data [119] -3.1 kA/m
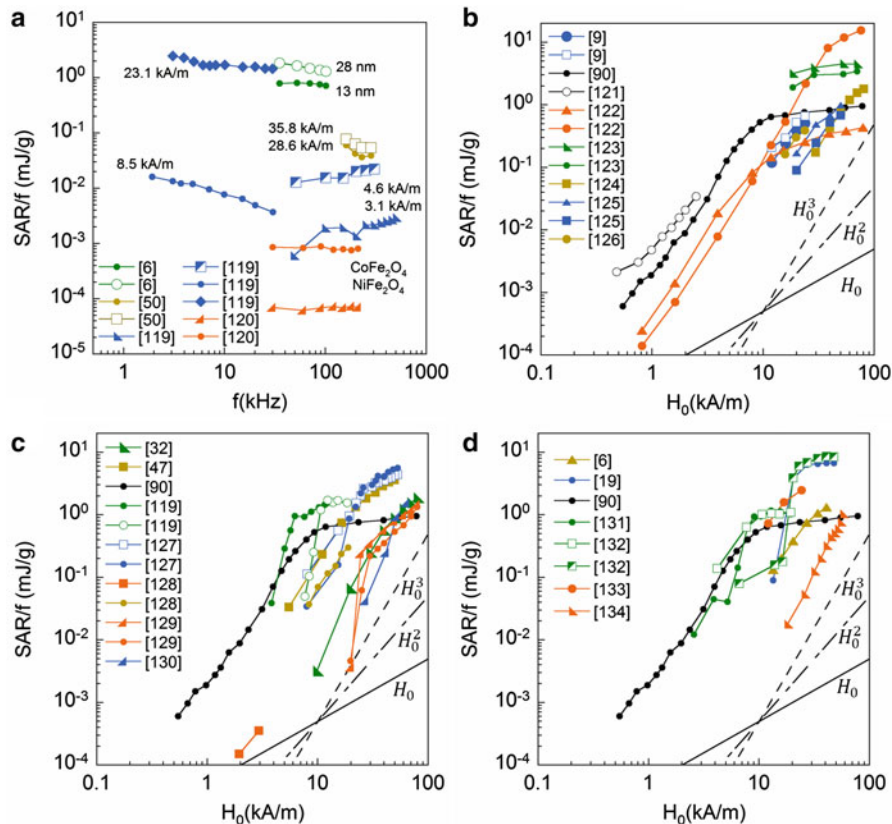
Fig. 8.6 SAR of FM-SD MNPs: (**a**) effect of f at constant H_0, size; (**b, c,** and **d**) effect of H_0 at constant f and size for iron oxide (**b**) and non-iron-oxide (**c, d**) MNPs. Curves aiding to identify H_0, H_0^2, and H_0^3 dependencies are also included

and [119] -4.6 kA/m, recorded with $H_0 < H_C$. Figure 8.6 also shows the variation of SAR/f with H_0 for iron oxide (b) and non-iron-oxide (c, d) FM-SD particles. Similar trends than those of Figs. 8.4 and 8.5 are found, and especially for non-iron-oxide materials, we observe curves revealing high H_C values and outstanding SAR/f values for $H_0 > H_C$.

5.2.4   Biological Limits of f and H_0

The above results and discussion help answering the two questions posed at the beginning of Sect. 5.2. On the one hand, most of the SAR value range found in the literature could be reliable even for the same material, given that correct f and H_0 values *are* supplied with these data. But, on the other hand, appealing SAR values of up to 10^4 W/g may not be more suitable for magnetic hyperthermia than those showing overlookable SAR values of 1 W/g, if they are achieved with H_0 values well

Table 8.3 Experimental details of the data collected in Fig. 8.6

References	Material	Size (nm)	Medium	f (kHz)	H_0 (kA/m)
[6]	$CoFe_2O_4$	13	Water	35–101	40.6
		28	Water	35–101	40.6
		28	Water	101	13.4–40.7
[9]	Fe_3O_4 nanocubes	20	DMSO + water	765	11.9–23.9
	Fe_3O_4 spheres	20	DMSO + water	765	11.9–23.9
[19]	FeC	13.6	Liquid	54	13.4–47.8
[32]	Fe	25	Water	128	9.8–80.1
[47]	$Co_{0.2}Fe_{2.8}O_4$	20	Water	117	5.5–49.8
[50]	Ocean Nanotech SHN-50 (Fe_3O_4)	50	Agar	161–284	28.6/35.8
[119]	FeCo	14.2	THF	48–500	3.1
				50–306	4.6
				2–30	8.5
				3–30	23.1
				2	3.8–11.5
				100	5.2–23.0
[120]	$CoFe_2O_4$	26.5	Powder	30–210	6.4
	$NiFe_2O_4$	24.8	Powder	30–210	6.4
[121]	Magnetosomes Fe_3O_4	34	Water + HEPES	750	0.5–2.5
[122]	Iron oxide	>10	Powder	0.05	0.8–789.5
[123]	Magnetosomes Fe_3O_4	45	Water	198	18.5–70.2
	Isolated Fe_3O_4	45	Water	198	18.5–70.2
[124]	Fe_2O_3	130 and 5	Water	120	10–80
[125]	$Fe_2O_3@SiO_2$	17	Agar	233	10–50
	Fe_2O_3 + 35Ag@SiO_2	15	Agar	233	10–50
[126]	Fe_3O_4 + Fe_2O_3	40	Water	765	15.8–23.7
[127]	Fe	11.3	Mesitylene	300	8–52.9
		16.3	Mesitylene	300	8–52.9
[128]	Fe	75	Epoxy	109	2.0/3.0
			Water	765	8.3–18.9
[129]	Co	27	Water + Albumin	120	0–100
	Ni	20	Water + Albumin	120	0–100
[130]	$CoFe_2O_4$	18	Agarose	108	27.0–66-6
[131]	FeCo	5.5 and 12.8	THF	56	2.6–19.4
[132]	FeCo	12.8	Liquid	54	4.2–19.4
	Fe@ Fe_xC_y	14.6	Liquid	54	6.6–47.5
[133]	$ZnFe_2O_4$	26.5	Water	240	12.1–24.2
[134]	$Zn_{0.2}Fe_{2.8}O_4$	55	Water	260	18.1–57.7

above the safety limits. This is especially true for FM MNPs with H_C values that overcome these limits. The question is: where are those limits?

The deleterious effects of AMF in the f, H_0 range suitable for hyperthermia have not been systematically studied. Hence, the exposure limits of patients during

hyperthermia therapies are not well established. The dominant physiological adverse response under AMF between 100 and 1000 kHz is the nonspecific temperature increase due to the induction of eddy currents in the tissue, which can lead to burns and blisters in extreme cases. The power dissipation due to Joule losses depends on f and H_0, the duration of the exposure, the electrical conductivity of the tissue, and the external radius, i.e., larger and more conductive parts of the body will generate more heat due to eddy currents. For this reason, the limbs usually tolerate higher f, H_0 values than other parts of the body. Other complications are muscle stimulations, including cardiac stimulation or arrhythmia.

In general, the tolerated H_0 decreases with increasing f, more or less steeply depending on the f range. The guidelines from the International Commission on Non-Ionizing Radiation Protection establish that for frequencies between 65 and 1000 kHz the $f \cdot H_0$ product should not exceed 1.6 kHz · kA/m. However, this reference level is a very conservative limit, focused on protect people from everyday exposure to radiation. A more widespread limit within the magnetic hyperthermia community is the product $f \cdot H_0 = 485$ kHz · kA/m, derived from the work of Atkinson et al. [135]. In this study, the patient comfort was evaluated increasing H_0 under a frequency of 13.56 MHz on the thorax. However, this product has to be taken as a rule-of-thumb for the order of magnitude of the fields involved in magnetic hyperthermia.

During the recent clinical studies on magnetic hyperthermia, a trial-and-error evaluation under medical supervision was carried out. Using a fixed AMF frequency of 100 kHz, the magnetic field strength was increased until the patients reported discomfort, to ensure the maximum possible heating ability for the injected MNPs. In clinical trials on prostate cancer [136], 10 patients experienced discomfort at $H_0 > 4$ kA/m, corroborating the Atkinson limit. However, the H_0 tolerated in the treatment of glioblastoma multiforme (brain tumor) went from 3.8 to 13.5 kA/m in a group of 14 patients [137]. Obviously, in these studies the sensitivity of the patients is also another variable.

In spite of the lack of exhaustive and reliable guidelines for the application of AMF in humans, the above experimental evidences lead to be conservative and expect that H_0 values higher than 15 kA/m with f in the 100–500 kHz range are probably not suitable for human application or, at least, for all parts of the human body. Coming back to Figs. 8.3 and 8.6, it can be concluded that some of the experimental results, especially those with the most outstanding SAR values, are obtained at probably too high H_0 values for human application, and that given the difficulties found for their extrapolation to lower H_0 values, they may not be that interesting for magnetic hyperthermia.

5.3 Interest of Measuring SAR as a Function of Temperature

Given that magnetic hyperthermia therapy involves temperatures from 36 up to about 50 °C, it is essential to evaluate SAR in this particular temperature range. As seen in the previous sections, the heating ability at given H_0, f values is

determined by the magnetic state of the MNP, which in turn depend on temperature. Some materials may show a weak SAR variation in this range, making reasonable the use of average values for therapy planning. But in other cases, SAR values may change appreciably as temperature increases, and applications may require the use of SAR(T) functions. Moreover, the determination of SAR does not need to be restricted to this narrow temperature range, since measurements over wider T ranges may provide valuable information about the magnetic state of the MNPs, which is helpful to the optimization of MNP heating ability.

Regarding magnetic detection, some SQUID magnetometers allow measuring hysteresis loops and ac-susceptibility in a wide T range (1.8 K to 1000 K). Also, some homemade setups [27, 39, 138] have succeeded in performing dynamic magnetic measurements up to 50 K above room temperature. Among calorimetric methods, the pulse heating method in adiabatic conditions is able to determine SAR (T) in the 120–370 K range [139, 140].

5.3.1   Self-regulating MNPs

The control of the maximum temperatures acquired by the tissues during the hyperthermia therapy is an open problem nowadays. In pursue of giving a solution to this problem, the so-called self-regulating MNPs have been considered. Such self-regulation is based on the transition undergone by FM materials at the Curie temperature, T_C. When $T > T_C$ the nanoparticles become paramagnetic and stop releasing heat, as no hysteresis can take place. By modifying the chemical composition of some MNPs, their T_C can be tuned so that it is located right above the maximum temperature desired for therapeutic hyperthermia. Such particles would then self-regulate the temperature during the therapy.

This is the case, for example, of lanthanum manganites such as $La_{1-x}Ag_yMnO_{3+\delta}$ [39] or $La_{1-x}Sr_xMnO_{3+\delta}$ [140]. The SAR(T) of those MNPs was measured, between 20 and 50 °C using magnetic methods in the former and between −20 and 100 °C by the pulse heating method in adiabatic conditions in the later. In both cases, SAR(T) characterization allowed finding a dissipation peak right below T_C, assigned to a Hopkinson peak, giving experimental evidence to the theoretical predictions of this phenomenon in MNPs [141]. Also, a sharp reduction in SAR was observed at T_C. Figure 8.7a shows this behavior for $La_{1-x}Sr_xMnO_{3+\delta}$ MNPs with different T_C values. Field-cooled $M(T)$ curves are also depicted in the figure to show the magnetic transition at T_C. This accurate SAR(T) determination also allowed relating the unexpected maximum temperatures achieved in nonadiabatic heating experiments with the thermal losses of the experimental system and the MNP heating ability [140].

5.3.2   Location of the FM/SMP Transition

As concluded in Sect. 5.2, MNPs with sizes next to the SPM/FM limit are the most suitable for low-H_0 applications. This optimum MNP volume (Eq. 8.13) depends on f and K and takes place at a given T_B. Then, for a fixed frequency, $\chi''(T)$ measurements may be used to determine T_B, since at this temperature χ'' presents a peak (Eq. 8.11). The location of T_B helps to conclude whether smaller (if $T_B > 36$ °C) or
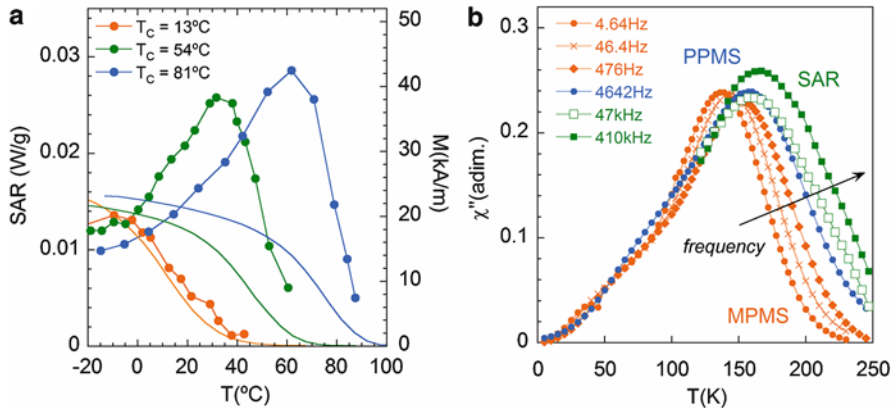
Fig. 8.7 (**a**) *Lines*: field-cooled $M(T)$ of $La_{1-x}Sr_xMnO_{3+\delta}$ MNPs with different T_C values, recorded with $H = 4$ kA/m. *Lines + symbols*: SAR(T) of the same samples measured by the pulse heating method in adiabatic conditions, with $H_0 = 2$ kA/m and $f = 108$ kHz (Adapted from Ref. [140]). (**b**) Temperature dependence of the out-of-phase ac magnetic susceptibility obtained from magnetic measurements (MPMS, 4.64–476 Hz, and PPMS, 4642 Hz) and from calorimetric measurements (SAR, 47 and 410 kHz). $\chi''(T)$ was calculated from the SAR(T) measurements using Eq. 8.2 (Adapted from Ref. [139])

larger (if $T_B < 36\,°C$) MNPs will optimize SAR for hyperthermia applications, thus serving as feedback for the synthesis of optimized MNPs. In the low-field range where the LRT applies (Eq. 8.3), SAR is linearly proportional to χ'' (Eq. 8.2) and $\chi''(T)$ provides equivalent information than SAR(T).

Figure 8.7b shows the good agreement between $\chi''(T)$ and SAR(T) measurements on a system of iron oxide nanoparticles. $\chi''(T)$ was determined using the MPMS and PPMS devices from Quantum Design Inc., and SAR(T) was obtained by the pulse heating method in adiabatic conditions [139]. The clear advantage of calorimetric SAR(T) measurements is that the AMF parameters used are typical of magnetic hyperthermia.

Eventually, when the H_0 values overcome the limits of the LRT, and the relationship between χ'' and SAR is unclear, it becomes evident that the direct determination of SAR(T) will provide more reliable information than χ'' about the temperature at which the dissipation peak takes place.

5.3.3 Dynamic Effects in Ferrofluids

The quantification of SAR at laboratory level is mainly performed on ferrofluids. However, in magnetic hyperthermia, MNPs are not dispersed in liquid, but trapped inside solid matrices (tissues). This may drive to discrepancies between the measured SAR values and the real MNP heating performance during therapies.

One possible source of discrepancy is the Brown relaxation mechanism. This is, like Néel relaxation, a thermally induced magnetization relaxation mechanism. The difference between them is that in Néel relaxation the magnetic moment reverses but the particle is fixed, while in Brown relaxation the whole MNP reverses. Both
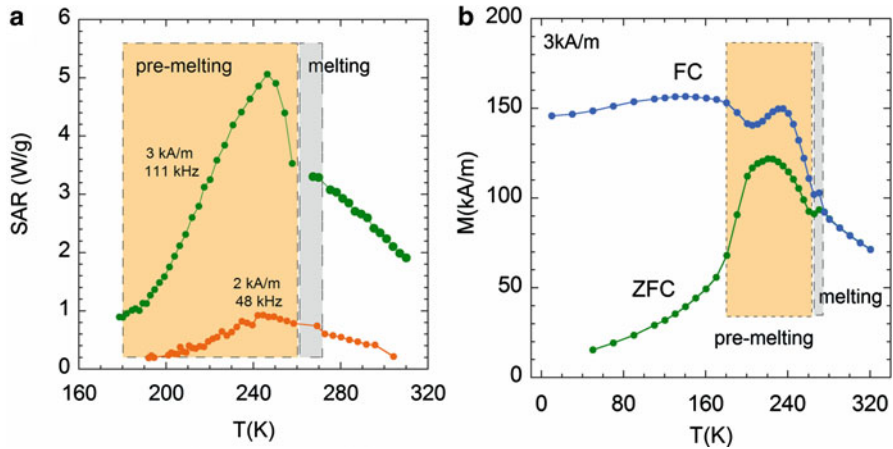
Fig. 8.8 (**a**) SAR(T) of Fe_3O_4 MNPs dispersed in n-dodecane, measured by the pulse heating method in adiabatic conditions under two different AMFs. (**b**) ZFC(*green*)/FC(*blue*) $M(T)$ of the same sample measured under a static magnetic field of 3 kA/m

mechanisms take place in parallel and it is the faster one which dominates dissipation. In general, Brown relaxation is only relevant for large MNPs.

However, other effects may occur. MNPs dispersed in a liquid media can get reoriented or form structures, particularly when subjected to a magnetic field [127, 142]. In general, the formed structures depend on the properties of the MNPs, dispersive media, H_0 and f, and will affect the heating ability of the assembly, as will be later explained in Sect. 5.4. SAR(T) measurements can unveil these processes [11, 143]. For example, Fig. 8.8a shows the SAR(T) of an assembly of Fe_3O_4 nanoparticles dispersed in n-dodecane, measured by the pulse heating method in adiabatic conditions. The sample presents a sharp heating peak below the melting temperature of the solvent and a trend change above the melting. This peak is a consequence of the premelting of the solvent at the interface between the particles and the dispersive media. The formed viscous layer allows the MNP to rotate and get oriented along the applied magnetic field, producing an increased magnetization (and SAR) with respect to that of the randomly oriented case. The increase of the magnetization at the premelting stage also appears in zero-field-cooled/field-cooled (ZFC/FC) $M(T)$ measurements (Fig. 8.8b) under a static magnetic field. However, both figures are not fully comparable, since SAR is consequence of a dynamic magnetic field.

## 5.4 Influence of Magnetic Nanoparticle Concentration and Arrangement

All the theoretical considerations made in previous sections about the effect of f, H_0, and T on SAR can be strictly applied to a single MNP or, in other words, to a system

of noninteracting MNPs. However, due to the magnetic nature of these particles, magnetic interparticle interactions are unavoidable. As MNPs are usually covered with a surfactant, they have no physical contact and thus the most relevant interparticle interaction is the dipolar one. Since dipolar interactions are long range in nature, a minimum interparticle distance of about 20 times the particle diameter is needed (volume concentration of 0.01 %) to achieve a noninteracting MNP system [144]. Such low concentrations are nonrealistic in magnetic hyperthermia. It has been observed that, when biocompatible MNPs are internalized by the cells, they are usually enclosed in vesicles containing hundreds of closely packed particles [145]. So even if the average volume concentration in the cell is low, the local concentration at the vesicles may be very high. The study of the effect of interparticle interactions on SAR is thus relevant for magnetic hyperthermia, since the SAR of MNPs well dispersed on ferrofluids can differ from that of densely packed arrangements.

The effect of magnetic interactions is modifying the energy barrier established by the magnetic anisotropy of the individual MNPs (Eq. 8.12). This explains that MNPs with lower anisotropy energy (i.e., $MnFe_2O_4$) are more affected by interparticle interactions than those with high anisotropy energy (i.e., $CoFe_2O_4$). Most analytical models including interparticle interactions deal with the calculation of a modified energy barrier, E_b, and the direct computation of τ [146–152]. Except for Ref. [148], all analytical models predict an increase of E_b and thus τ, with magnetic interactions, leading to an increase of the blocking temperature, T_B. But although the calculation of $\tau(T)$ gives useful information about T_B, the relaxation time alone does not give direct information on SAR, unless analytical or empirical expressions are obtained relating both quantities in the case of magnetic interactions.

When considering realistic assemblies with millions of individual particles, developing an analytical theoretical framework is an extremely challenging task. Dipolar interactions are long-ranged and depend on the relative orientation of the MNP magnetic moments and on the interparticle distances. For this reason, the theoretical consideration of magnetic interactions has been recently carried out by means of numerical simulations of the hysteresis cycles. Most simulations deal with assemblies of randomly distributed MNPs also with random easy axis distribution, dispersed in a solid matrix (i.e., the position and orientation of the MNPs are fixed). In these conditions, the effect of magnetic interactions on the heating ability of the MNPs will depend on the state of the particle (i.e., FM-SD or SPM-SD), the amplitude of the applied field, the average distance between MNPs, and the intrinsic properties of the particles: size, shape, polydispersity, M_S, and K.

Neglecting the effect of f, the static hysteresis loops of systems of randomly distributed nanoparticles in the FM-SD regime have been simulated at different MNP volume concentrations [128]. Figure 8.9a depicts the obtained results. It is observed that the behavior of SAR/f with interaction strength was found to depend on H_0: for low fields, increasing the interaction strength increased SAR/f, while for fields above $H_C \cong 0.48 \cdot H_K$, SAR/f decreased with increasing interactions. Moreover, the interactions increased the field at which saturation of SAR/f occurred.
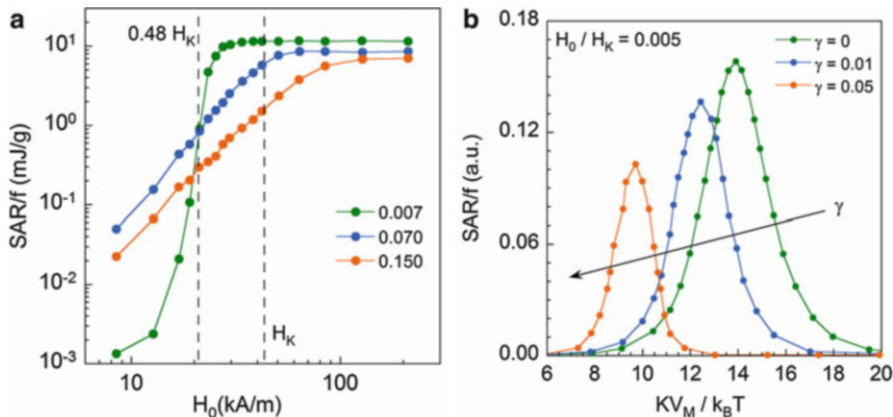
Fig. 8.9 (**a**) Numerical simulation of the variation of SAR/f on H_0 for the same FM-SD MNPs with different volume concentrations (Adapted from Ref. [128]). *Dashed lines* indicate the position of H_C ($\cong 0.48\, H_K$) and H_K. (**b**) Numerical simulation of SAR of SD MNPs as a function of KV_M/k_BT at fixed f, V_M and M_S at different values of the interaction parameter γ and low H_0 (Adapted from Ref. [153]). The *arrow* indicates the direction of increasing concentration

Dynamic hysteresis loops have been also numerically simulated [153] to calculate the SAR of SD particles as a function of KV_M/k_BT at a fixed f and high and low H_0, using a mean field approximation. In this work, the strength of the interactions is quantified by the parameter γ, being $\gamma = 0$ the noninteracting case. Figure 8.9b displays the obtained results for low H_0 values. A displacement of T_B towards higher temperatures takes place with increasing magnetic interactions. To illustrate the effect of this displacement on SAR, let us consider a MNP system tested at 36 °C. If this system is in the SPM regime ($T_B < 36$ °C) in the noninteracting case, decreasing interparticle distances leads to an initial increase of SAR ($T_B \cong 36$ °C), steeper in the case of low H_0, followed by a decrease of SAR ($T_B > 36$ °C), since the MNP system enters the FM state. Consequently, if the size of a MNP system has been designed to show optimum heating ability at 36 °C in the noninteracting case, the presence of magnetic interactions can drive the energy barrier of the system out of the optimum value, thus diminishing the SAR. Figure 8.9b also shows that the value of the maximum SAR (height of the curves) decreases with increasing γ.

Variations of SAR with concentration have also been found experimentally. For example, the SAR at 3 kA/m ($H_0 < H_K$) and 109 kHz of Fe_2O_3 ferrofluids in the SPM regime decreased a 57 % with increasing volume concentration from 0.04 % to 0.18 % [154]. Also, the SAR of polydisperse Fe_3O_4 MNPs suspensions in the SPM regime was found to decrease with increasing volume concentrations up to 6.6 % under AMFs with $f = 1500$ kHz and $H_0 < H_K$ [104]. The SAR of Fe_3O_4 suspensions of magnetite MNPs of different sizes measured under $H_0 > H_C$ at

765 kHz [93] was reported to behave differently at increasing concentration (0.15–1.2 mg/ml) depending on their size, in qualitative accordance with simulations in Ref. [153]. In contrast to previous results, a concentration-independent SAR was found for Fe_2O_3 suspensions in water with different mean sizes measured under $H_0 < H_C$ and 522.7 kHz with increasing concentration from 5 to 260 mg_{Fe}/ml [96].

This variety of theoretical and experimental results reflects the intrinsic complexity of the problem. But there is a further factor increasing difficulty: MNP arrangement. The above-referred works make the assumption that an increase in concentration leads to a homogeneous decrease of the interparticle distance, i.e., that the MNPs are homogeneously distributed in the dispersive media. However, in most systems, the interparticle distance is not controlled, and concentration is just a statistical value. In dispersion, MNPs can form aggregates, columns, chains, rings, etc. In sum, a wide variety of 1D, 2D, or 3D structures. This can occur in absence or presence of either a static or an alternating magnetic field [132]. And it has been found that such arrangements influence the heating ability of a MNP system in a different way than homogeneous concentration.

Recent numerical simulations on chains of SPM nanoparticles [155] point to a reduction of the maximum SAR and a shifting of T_B towards higher temperatures as the chain length increases, while simulations of MNP chains well within the FM regime [156] reveal that the maximum SAR value at high H_0 values grows as the chain length increases, as well as the required H_0 value to achieve this high SAR. Eventually, numerical simulations of anisotropic columns of 6x6 particles and increasing length under saturating fields $H_0 > H_K$ [132] predict an increase of SAR with interactions for low K particles, while a reduction for high K particles. These three works [132, 155, 156] show also experimental results with good qualitative agreement with their simulations.

These studies, together with others on clusters and rings [156–158], highlight the nonnegligible influence of the MNP arrangement on the heating ability of MNP systems, which should not be overlooked. Given that at present it is not possible to predict the geometrical arrangement that MNPs will adopt in tissues, maybe the fabrication of nanoobjects preserving a favorable MNP superstructure would be a promising path to achieve MNP assemblies whose SAR will scarcely vary once they are internalized by cells [159].

6   Conclusions and Future Perspective

The heat generated by certain magnetic nanoparticles under the action of adequate alternating magnetic fields is used as active principle in the magnetic hyperthermia cancer therapy. A successful localized therapy must be able to provide therapeutic temperatures in tumors, while keeping reasonable low temperatures in the healthy tissue. In addition, the parameters of the applied AMF should

be limited to human-tolerated values, although these values are only roughly defined at present.

Obtaining precise SAR values of the used MNPs is necessary to determine the spatial and temporal temperature evolution of the maximum temperatures acquired during the therapies. This implies using experimental setups and methods deriving the most accurate results. It has been concluded that the methods using magnetic detection often derive highly accurate data, but the main drawback of commercial setups is that they operate with H_0, f values not suitable for magnetic hyperthermia. However, recent homemade magnetometers and susceptometers are starting to overcome this problem. With respect to calorimetric methods, the widely used initial-slope method in isoperibol conditions often derives unquantified inaccuracies due to the disagreement between the theoretical assumptions of the thermal model and the experimental setups and measuring conditions. Eventually, the only realization of a setup capable of determining SAR by the pulse heating method in adiabatic conditions has proven the good accuracy of the method, considered the only "absolute" method in adiabatic calorimetry.

Furthermore, several factors affect the heating ability of MNPs and must be therefore taken into account when evaluating SAR. Among them, the parameters of the applied AMF can make the SAR of the same MNP vary several orders of magnitude. SAR increases with H_0 and f, since more electromagnetic energy is absorbed by the MNP and afterwards released as heat. But the dependencies of SAR on these parameters are not straightforward and vary with the magnetic state of the MNP. Such dependencies have been studied through the area of the dynamic hysteresis loop described in each AMF cycle, SAR/f. It has been shown that for SD MNPs whose blocking temperature is near the temperature of interest ($\cong 36\,°C$) for magnetic hyperthermia, i.e., MNPs that are near the FM/SPM transition at 36 °C, SAR/f depends on H_0^2 if H_0 is low enough as to fulfill the LRT condition. For higher H_0 values, SAR/f varies as H_0^n, with n ranging between 1.8 and 2.5. When H_0 is sufficiently high ($H_0 > H_k$) so that major loops are described, SAR becomes independent of H_0. For FM-SD MNPs ($T_B >> 36\,°C$), SAR/f is found to be negligible for $H_0 < H_C$. For $H_C < H_0 < H_k$, SAR experiments a sharp increase, following a H_0^n law with n values up to even 60. For $H_0 > H_k$ SAR/f saturates (major loops). These dependencies drive to two main conclusions: (i) SAR data obtained at a particular H_0 value are not easily extrapolable to other H_0 values, so that it is imperative to determine SAR with the H_0 values suitable for magnetic hyperthermia; (ii) MNPs with sizes next to the SPM/FM limit at 36 °C are suitable for low-H_0 applications (e.g., prostate cancer), while larger particles should be used for higher fields, provided that their H_C value do not overcome the H_0 limit for biological application. The variation of SAR/f with f, while being less pronounced than that of H_0, is nonnegligible, nonextrapolable, and also dependent on the MNP magnetic state.

SAR must be evaluated between 36 up to about 50 °C, and in the general case, the use of SAR values averaged over this T range may be reasonable for planning the

therapies. However, in some cases, SAR values may change appreciably as temperature increases as, for example, in self-regulating MNPs, so that SAR(T) data must be used. In addition, the determination of SAR over wider T ranges may provide valuable information, such as the location of the FM/SPM transition, helpful to the optimization of MNP heating ability at low H_0 values, or the presence of dynamic effects of MNPs in fluids, leading to an overestimation of their heating ability compared to its in vivo performance.

Also, many analytical and numerical models neglect the unavoidable magnetic interparticle interactions, given the MNP concentrations involved in magnetic hyperthermia. But recently, many studies have highlighted the great influence of this phenomenon in SAR. Among them, dipolar interaction is the most relevant in MNPs systems. This is a long-range interaction which depends on the relative orientation of the MNP magnetic moments and on the interparticle distances, so that computing its effects in realistic systems with millions of individual particles is a hard task. Different analytical models, numerical simulations, and experimental measurements have revealed the complexity of this problem. Dipolar interactions modify the energy barrier established by the magnetic anisotropy of the individual MNPs and, in general, generate a decrease in SAR, although some magnetic states of the noninteracting MNPs may result in a SAR increase under moderate interaction strength. In addition, the formation of different 1D, 2D and 3D arrangements of MNPs increases difficulty, since it has been found that such arrangements influence SAR differently than MNP arrangements with homogeneous interparticle distances.

The study of the influence of the concentration and arrangement of MNPs in SAR is expected to remain a very active research line in the next future, since it aims at reducing the often encountered discrepancies between the SAR values, usually measured in ferrofluids, and the temperature distributions acquired in hyperthermia applications, in which MNPs are internalized by cells and often confined in densely packed vesicles. In this sense, a more accurate determination of SAR on more adequate arrangements (e.g., solid matrices, phantoms, biopsies) would improve the accordance between simulations and real temperatures during therapies. Also, the development of further numerical simulations deriving general trends and conclusions would help increasing this accordance. And, eventually, the use of nanoobjects with an initial favorable MNP arrangement could also aid reducing these discrepancies, as well as the deleterious effects of the uncontrolled arrangement of MNPs on SAR.

7 Tables of Acronyms and Symbols

See Tables 8.4 and 8.5

Table 8.4 Table of acronyms

Acronym	Name
AMF	Alternating magnetic field
FM-MD	Ferro/ferrimagnetic multi-domain
FM-SD	Ferro/ferrimagnetic single-domain
LRT	Linear response theory
MNP	Magnetic nanoparticle
SAR	Specific absorption rate
SLP	Specific loss power
SQUID	Superconducting quantum interference device
SPM-SD	Superparamagnetic single-domain
VSM	Vibrating sample magnetometer
ZFC/FC	Zero-field-cooled/field-cooled

Table 8.5 Table of physical quantity symbols

Symbol	Name
H_0	AMF amplitude
H_K	Anisotropy field
E_{hys}	Area of the hysteresis loop
τ_0	Attempt time
T_B	Blocking temperature
k_B	Boltzmann constant
L	Coefficient accounting for linear thermal losses
H_C	Coercive field
T_C	Curie temperature
Δt	Duration of AMF application
E_{b0}	Energy barrier for magnetization reversal
f	Frequency of the AMF
C	Heat capacity of the sample
P	Heat power generated by the MNPs
β	Initial slope of the exponential $T(t)$ in isoperibol conditions
χ'	In-phase component of χ
K	Magnetic anisotropy constant
H	Magnetic field strength
τ	Magnetic moment relaxation time
χ	Magnetic susceptibility
M	Magnetization
ρ_b	Mass density of the blood
ρ_{MNP}	Mass density of the MNPs
ρ	Mass density of the sample/tissue
m_{MNP}	Mass of magnetic material
$T_{\max}$	Maximum achieved T in isoperibol conditions
$\Delta T_{\max}$	Maximum temperature increase in isoperibol conditions
P_m	Metabolic heat power

(*continued*)

Table 8.5 (continued)

Symbol	Name
E_b	Modified energy barrier for magnetization reversal
τ_N	Néel relaxation time
t_0	Onset of the AMF application
$V_M{}^{Opt}$	Optimum MNP volume corresponding to the SPM/FM transition
χ''	Out-of-phase component of χ
γ	Parameter accounting for magnetic interactions in Ref. [153]
κ	Parameter modifying H_C in Ref. [118]
W_b	Perfusion constant
μ_0	Permeability of free space
M_s	Saturation magnetization
c_b	Specific heat capacity of the blood
c	Specific heat capacity of the sample/tissue
χ_0	Static susceptibility
ΔT	Temperature increment of the sample during Δt in adiabatic conditions
T_b	Temperature of the blood
T_0	Temperature of the sample environment
T	Temperature of the sample/tissue
k	Thermal conductivity of the sample/tissue
τ_i	Time constant of the exponential $T(t)$ in isoperibol conditions
t_m	Time elapsed between the fields H and $H + \Delta H$ during the hysteresis loop
V_M	Volume of a MNP

References

1. Eurostat (2014) Causes of death statistics- statistics explained. http://epp.eurostat.ec.europa.eu/statistics_explained/index.php/Causes_of_death_statistics
2. NCHS (2014) FastStats- leading causes of death. www.cdc.gov/nchs/fastats/leading-causes-of-death.htm
3. van der Zee J (2002) Heating the patient: a promising approach? Ann Oncol 13(8):1173–1184
4. Gilchrist R, Meda R, Shorey WD, Hanselman RC, Parrott JC, Taylor CB (1957) Selective inductive heating of lymph nodes. Ann Surg 164(4):596–606
5. MagForce (2015) NanoTherm therapy. www.magforce.de/en/produkte.html
6. Mazario E, Menéndez N, Herrasti P, Cañete M, Connord V, Carrey J (2013) Magnetic hyperthermia properties of electrosynthesized cobalt ferrite nanoparticles. J Phys Chem C 117(21):11405–11411
7. Kumar CSSR, Mohammad F (2011) Magnetic nanomaterials for hyperthermia-based therapy and controlled drug delivery. Adv Drug Deliv Rev 63(9):789–808
8. Mehdaoui B, Meffre A, Carrey J, Lachaize S, Lacroix L-M, Gougeon M, Chaudret B, Respaud M (2011) Optimal size of nanoparticles for magnetic hyperthermia: a combined theoretical and experimental study. Adv Funct Mater 21(23):4573–4581
9. Martinez-Boubeta C, Simeonidis K, Makridis A, Angelakeris M, Iglesias O, Guardia P, Cabot A, Yedra L, Estrade S, Peiro F, Saghi Z, Midgley PA, Conde-Leboran I, Serantes D, Baldomir D (2013) Learning from nature to improve the heat generation of iron-oxide nanoparticles for magnetic hyperthermia applications. Sci Rep 3:1652

10. Noh S-h, Na W, Jang J-T, Lee J-H, Lee EJ, Moon SH, Lim Y, Shin J-S, Cheon J (2012) Nanoscale magnetism control via surface and exchange anisotropy for optimized ferrimagnetic hysteresis. Nano Lett 12(7):3716–3721

11. Andreu I, Natividad E, Ravagli C, Castro M, Baldi G (2014) Heating ability of cobalt ferrite nanoparticles showing dynamic and interaction effects. RSC Adv 4(55):28968–28977

12. Nanotherics (2015) magneThermTM. www.nanotherics.com/magnetherm.htm

13. Natividad E, Castro M, Mediano A (2008) Accurate measurement of the specific absorption rate using a suitable adiabatic magnetothermal setup. Appl Phys Lett 92(9):093116

14. Luong TT, Ha TP, Tran LD, Do MH, Mai TT, Pham NH, Phan HBT, Pham GHT, Hoang NMT, Nguyen QT, Nguyen PX (2011) Design of carboxylated Fe_3O_4/poly(styrene-co-acrylic acid) ferrofluids with highly efficient magnetic heating effect. Colloids Surf A 384(1–3):23–30

15. Connord V, Mehdaoui B, Tan RP, Carrey J, Respaud M (2014) An air-cooled Litz wire coil for measuring the high frequency hysteresis loops of magnetic samples – a useful setup for magnetic hyperthermia applications. Rev Sci Instrum 85(9):093904

16. Ma M, Wu Y, Zhou J, Sun Y, Zhang Y, Gu N (2004) Size dependence of specific power absorption of Fe_3O_4 particles in AC magnetic field. J Magn Magn Mater 268(1–2):33–39

17. Kawashita M, Tanaka M, Kokubo T, Inoue Y, Yao T, Hamada S, Shinjo T (2005) Preparation of ferrimagnetic magnetite microspheres for in situ hyperthermic treatment of cancer. Biomaterials 26(15):2231–2238

18. Kasuya R, Kikuchi T, Mamiya H, Ioku K, Endo S, Nakamura A, Takai T, Balachandran J (2010) Heat dissipation characteristics of magnetite nanoparticles and their application to macrophage cells. Phys Procedia 9:186–189

19. Meffre A, Mehdaoui B, Kelsen V, Fazzini PF, Carrey J, Lachaize S, Respaud M, Chaudret B (2012) A simple chemical route toward monodisperse iron carbide nanoparticles displaying tunable magnetic and unprecedented hyperthermia properties. Nano Lett 12(9):4722–4728

20. Jones SK, Winter JG (2001) Experimental examination of a targeted hyperthermia system using inductively heated ferromagnetic microspheres in rabbit kidney. Phys Med Biol 46 (2):385

21. Alphandéry E, Faure S, Seksek O, Guyot F, Chebbi I (2011) Chains of magnetosomes extracted from AMB-1 magnetotactic bacteria for application in alternative magnetic field cancer therapy. ACS Nano 5(8):6279–6296

22. Dennis CL, Ivkov R (2013) Physics of heat generation using magnetic nanoparticles for hyperthermia. Int J Hyperthermia 29(8):715–729

23. Buschow KHJ, de Boer FR (2003) Physics of magnetism and magnetic materials. Kluwer Academic, Plenum, New York

24. Rosensweig RE (2002) Heating magnetic fluid with alternating magnetic field. J Magn Magn Mater 252:370–374

25. Fiorillo F (2010) Measurements of magnetic materials. Metrologia 47(2):S114

26. McElfresh M (1994) Fundamentals of magnetism and magnetic measurements. Quantum Design, San Diego

27. Beković M, Trlep M, Jesenik M, Goričan V, Hamler A (2013) An experimental study of magnetic-field and temperature dependence on magnetic fluid's heating power. J Magn Magn Mater 331:264–268

28. Carrey J, Mehdaoui B, Respaud M (2011) Simple models for dynamic hysteresis loop calculations of magnetic single-domain nanoparticles: application to magnetic hyperthermia optimization. J Appl Phys 109(8):083921

29. Holman J (1996) Heat transfer, Mcgraw-Hill series in mechanical engineering. McGraw Hill, New York, 752

30. Lartigue L, Hugounenq P, Alloyeau D, Clarke SP, Lévy M, Bacri J-C, Bazzi R, Brougham DF, Wilhelm C, Gazeau F (2012) Cooperative organization in iron oxide multi-core nanoparticles potentiates their efficiency as heating mediators and MRI contrast agents. ACS Nano 6 (12):10935–10949

31. Lee J-H, Jang J-T, Choi J-S, Moon SH, Noh S-H, Kim J-W, Kim J-G, Kim I-S, Park KI, Cheon J (2011) Exchange-coupled magnetic nanoparticles for efficient heat induction. Nat Nano 6 (7):418–422

32. Taylor A, Krupskaya Y, Krämer K, Füssel S, Klingeler R, Büchner B, Wirth MP (2010) Cisplatin-loaded carbon-encapsulated iron nanoparticles and their in vitro effects in magnetic fluid hyperthermia. Carbon 48(8):2327–2334

33. Kim D-H, Nikles DE, Brazel CS (2010) Synthesis and characterization of multifunctional chitosan- MnFe$_2$O$_4$ nanoparticles for magnetic hyperthermia and drug delivery. Materials 3 (7):4051–4065

34. Rovers SA, van der Poel LAM, Dietz CHJT, Noijen JJ, Hoogenboom R, Kemmere MF, Kopinga K, Keurentjes JTF (2009) Characterization and magnetic heating of commercial superparamagnetic iron oxide nanoparticles. J Phys Chem C 113(33):14638–14643

35. Shah SA, Hashmi MU, Alam S (2011) Effect of aligning magnetic field on the magnetic and calorimetric properties of ferrimagnetic bioactive glass ceramics for the hyperthermia treatment of cancer. Mater Sci Eng C 31(5):1010–1016

36. Zhang L-Y, Gu H-C, Wang X-M (2007) Magnetite ferrofluid with high specific absorption rate for application in hyperthermia. J Magn Magn Mater 311(1):228–233

37. Kobayashi H, Ueda K, Tomitaka A, Yamada T, Takemura Y (2011) Self-heating property of magnetite nanoparticles dispersed in solution. IEEE Trans Magn 47(10):4151–4154

38. Glöckl G, Hergt R, Zeisberger M, Dutz S, Nagel S, Weitschies W (2006) The effect of field parameters, nanoparticle properties and immobilization on the specific heating power in magnetic particle hyperthermia. J Phys Condens Matter 18(38):S2935

39. Atsarkin VA, Generalov AA, Demidov VV, Mefed AE, Markelova MN, Gorbenko OY, Kaul AR, Roy EJ, Odintsov BM (2009) Critical RF losses in fine particles of La$_{1-x}$Ag$_y$MnO$_{3+\delta}$: prospects for temperature-controlled hyperthermia. J Magn Magn Mater 321(19):3198–3202

40. Aono H, Ebara H, Senba R, Naohara T, Maehara T, Hirazawa H, Watanabe Y (2012) High heat generation ability in AC magnetic field for nano-sized magnetic Y$_3$Fe$_5$O$_{12}$ powder prepared by bead milling. J Magn Magn Mater 324(12):1985–1991

41. Sharma M, Mantri S, Bahadur D (2012) Study of carbon encapsulated iron oxide/iron carbide nanocomposite for hyperthermia. J Magn Magn Mater 324(23):3975–3980

42. Verde EL, Landi GT, Gomes JA, Sousa MH, Bakuzis AF (2012) Magnetic hyperthermia investigation of cobalt ferrite nanoparticles: comparison between experiment, linear response theory, and dynamic hysteresis simulations. J Appl Phys 111(12):123902

43. Comes Franchini M, Baldi G, Bonacchi D, Gentili D, Giudetti G, Lascialfari A, Corti M, Marmorato P, Ponti J, Micotti E, Guerrini U, Sironi L, Gelosa P, Ravagli C, Ricci A (2010) Bovine serum albumin-based magnetic nanocarrier for MRI diagnosis and hyperthermic therapy: a potential theranostic approach against cancer. Small 6(3):366–370

44. Asin L, Goya GF, Tres A, Ibarra MR (2013) Induced cell toxicity originates dendritic cell death following magnetic hyperthermia treatment. Cell Death Dis 4:e596

45. Bordelon DE, Cornejo C, Grüttner C, Westphal F, DeWeese TL, Ivkov R (2011) Magnetic nanoparticle heating efficiency reveals magneto-structural differences when characterized with wide ranging and high amplitude alternating magnetic fields. J Appl Phys 109 (12), Article 124904, p 8

46. Kline TL, Xu Y-H, Jing Y, Wang J-P (2009) Biocompatible high-moment FeCo-Au magnetic nanoparticles for magnetic hyperthermia treatment optimization. J Magn Magn Mater 321 (10):1525–1528

47. Kita E, Oda T, Kayano T, Sato S, Minagawa M, Yanagihara H, Kishimoto M, Mitsumata C, Hashimoto S, Yamada K, Ohkohchi N (2010) Ferromagnetic nanoparticles for magnetic hyperthermia and thermoablation therapy. J Phys D Appl Phys 43(47):474011

48. Khandhar AP, Ferguson RM, Simon JA, Krishnan KM (2012) Enhancing cancer therapeutics using size-optimized magnetic fluid hyperthermia. J Appl Phys 111(7), Article 07B306, p 4

49. Regmi R, Black C, Sudakar C, Keyes PH, Naik R, Lawes G, Vaishnava P, Rablau C, Kahn D, Lavoie M, Garg VK, Oliveira AC (2009) Effects of fatty acid surfactants on the magnetic and magnetohydrodynamic properties of ferrofluids. J Appl Phys 106(11), Article 113902, p 9

50. Li CH, Hodgins P, Peterson GP (2011) Experimental study of fundamental mechanisms in inductive heating of ferromagnetic nanoparticles suspension (Fe_3O_4 Iron Oxide Ferrofluid). J Appl Phys 110(5):054303

51. Drake P, Cho H-J, Shih P-S, Kao C-H, Lee K-F, Kuo C-H, Lin X-Z, Lin Y-J (2007) Gd-doped iron-oxide nanoparticles for tumour therapy via magnetic field hyperthermia. J Mater Chem 17 (46):4914–4918

52. Maity D, Chandrasekharan P, Pradhan P, Chuang K-H, Xue J-M, Feng S-S, Ding J (2011) Novel synthesis of superparamagnetic magnetite nanoclusters for biomedical applications. J Mater Chem 21(38):14717–14724

53. Salas G, Camarero J, Cabrera D, Takacs H, Varela M, Ludwig R, Dähring H, Hilger I, Miranda R, Morales MdP, Teran FJ (2014) Modulation of magnetic heating via dipolar magnetic interactions in monodisperse and crystalline iron oxide nanoparticles. J Phys Chem C 118(34):19985–19994

54. Salas G, Casado C, Teran FJ, Miranda R, Serna CJ, Morales MP (2012) Controlled synthesis of uniform magnetite nanocrystals with high-quality properties for biomedical applications. J Mater Chem 22(39):21065–21075

55. Khot VM, Salunkhe AB, Thorat ND, Ningthoujam RS, Pawar SH (2013) Induction heating studies of dextran coated $MgFe_2O_4$ nanoparticles for magnetic hyperthermia. Dalton Trans 42 (4):1249–1258

56. Shlyakhtin OA, Leontiev VG, Young-Jei O, Kuznetsov AA (2007) New manganite-based mediators for self-controlled magnetic heating. Smart Mater Struct 16(5):N35

57. Izydorzak M, Skumiel A, Leonowicz M, Kaczmarek-Klinowska M, Pomogailo AD, Dzhardimalieva GI (2012) Thermophysical and magnetic properties of carbon beads containing cobalt nanocrystallites. Int J Thermophys 33(4):627–639

58. Zhao D-L, Zhang H-L, Zeng X-W, Xia Q-S, Tang J-T (2006) Inductive heat property of Fe_3O_4/ polymer composite nanoparticles in an ac magnetic field for localized hyperthermia. Biomed Mater 1(4):198

59. Zhixia L, Masakazu K, Norio A, Michihide M, Masahiro H, Masaaki D (2010) Magnetic SiO_2 gel microspheres for arterial embolization hyperthermia. Biomed Mater 5(6):065010

60. Le Renard P-E, Lortz R, Senatore C, Rapin J-P, Buchegger F, Petri-Fink A, Hofmann H, Doelker E, Jordan O (2011) Magnetic and in vitro heating properties of implants formed in situ from injectable formulations and containing superparamagnetic iron oxide nanoparticles (SPIONs) embedded in silica microparticles for magnetically induced local hyperthermia. J Magn Magn Mater 323(8):1054–1063

61. Chen S-W, Lai J-J, Chiang C-L, Chen C-L (2012) Construction of orthogonal synchronized bi-directional field to enhance heating efficiency of magnetic nanoparticles. Rev Sci Instrum 83(6), Article 064701, p 7

62. Hilger I, Frühauf K, Andrä W, Hiergeist R, Hergt R, Kaiser WA (2002) Heating potential of iron oxides for therapeutic purposes in interventional radiology. Acad Radiol 9(2):198–202

63. Marcos-Campos I, Asín L, Torres TE, Marquina C, Tres A, Ibarra MR, Goya GF (2011) Cell death induced by the application of alternating magnetic fields to nanoparticle-loaded dendritic cells. Nanotechnology 22(20):205101

64. Pennes HH (1948) Analysis of tissue and arterial blood temperatures in the resting human forearm. J Appl Physiol 1(2):93–122

65. Fan J, Wang L (2011) Analytical theory of bioheat transport. J Appl Phys 109(10):104702

66. Golneshan AA, Lahonian M (2011) The effect of magnetic nanoparticle dispersion on temperature distribution in a spherical tissue in magnetic fluid hyperthermia using the lattice Boltzmann method. Int J Hyperthermia 27(3):266–274

67. Moroz P, Jones SK, Gray BN (2002) Magnetically mediated hyperthermia: current status and future directions. Int J Hyperthermia 18(4):267–284

68. Bordelon DE, Goldstein RC, Nemkov VS, Kumar A, Jackowski JK, DeWeese TL, Ivkov R (2012) Modified solenoid coil that efficiently produces high amplitude AC magnetic fields with enhanced uniformity for biomedical applications. IEEE Trans Magn 48(1):47–52

69. Bekovic M, Hamler A (2010) Determination of the heating effect of magnetic fluid in alternating magnetic field. IEEE Trans Magn 46(2):552–555

70. Huang S, Wang SY, Gupta A, Borca-Tasciuc DA, Salon SJ (2012) On the measurement technique for specific absorption rate of nanoparticles in an alternating electromagnetic field. Meas Sci Technol 23(3):035701

71. Pollert E, Knížek K, Maryško M, Kašpar P, Vasseur S, Duguet E (2007) New Tc-tuned magnetic nanoparticles for self-controlled hyperthermia. J Magn Magn Mater 316 (2):122–125

72. Aono H, Watanabe Y, Naohara T, Maehara T, Hirazawa H, Watanabe Y (2011) Effect of bead milling on heat generation ability in AC magnetic field of $FeFe_2O_4$ powder. Mater Chem Phys 129(3):1081–1088

73. Gudoshnikov SA, Liubimov BY, Usov NA (2012) Hysteresis losses in a dense superpara-magnetic nanoparticle assembly. AIP Adv 2(1):012143

74. Garaio E, Collantes JM, Garcia JA, Plazaola F, Mornet S, Couillaud F, Sandre O (2014) A wide-frequency range AC magnetometer to measure the specific absorption rate in nanoparticles for magnetic hyperthermia. J Magn Magn Mater 368:432–437

75. Ahrentorp F, Astalan AP, Jonasson C, Blomgren J, Qi B, Mefford OT, Yan M, Courtois J, Berret JF, Fresnais J, Sandre O, Dutz S, Müller R, Johansson C (2010) Sensitive high frequency AC susceptometry in magnetic nanoparticle applications. AIP Conf Proc 1311 (1):213–223

76. Nakamura K, Ueda K, Tomitaka A, Yamada T, Takemura Y (2013) Self-heating temperature and AC hysteresis of magnetic iron oxide nanoparticles and their dependence on secondary particle size. IEEE Trans Magn 49(1):240–243

77. Oireachtaigh CM, Fannin PC (2008) Investigation of the non-linear loss properties of magnetic fluids subject to large alternating fields. J Magn Magn Mater 320(6):871–880

78. Cobos P, Maicas M, Sanz M, Aroca C (2011) High resolution system for nanoparticles hyperthermia efficiency evaluation. IEEE Trans Magn 47(10):2360–2363

79. Gmelin E (1979) Modern low-temperature calorimetry. Thermochim Acta 29(1):1–39

80. Schnelle W, Gmelin E (2002) Critical review of small sample calorimetry: improvement by auto-adaptive thermal shield control. Thermochim Acta 391(1–2):41–49

81. Natividad E, Castro M, Mediano A (2009) Adiabatic vs. non-adiabatic determination of specific absorption rate of ferrofluids. J Magn Magn Mater 321(10):1497–1500

82. Wang S-Y, Huang S, Borca-Tasciuc D (2013) Potential sources of errors in measuring and evaluating the specific loss power of magnetic nanoparticles in an alternating magnetic field. IEEE Trans Magn 49(1):255–262

83. Hilger I (2013) In vivo applications of magnetic nanoparticle hyperthermia. Int J Hyperthermia 29(8):828–834

84. Krishnan KM (2010) Biomedical nanomagnetics: a spin through possibilities in imaging, diagnostics, and therapy. IEEE Trans Magn 46(7):2523–2558

85. Koksharov YA (2009) Magnetism of nanoparticles: effects of size, shape, and interactions. In Gubin SP (ed) Magnetic nanoparticles. Wiley-VCH, Weinheim, Germany, pp 197–254

86. O'Handley RC (2000) Modern magnetic materials: principles and applications. Wiley-VCH, Weinheim, Germany, p 768

87. Raikher YL, Stepanov VI, Perzynski R (2004) Dynamic hysteresis of a superparamagnetic nanoparticle. Physica B 343(1–4):262–266

88. Usov NA (2010) Low frequency hysteresis loops of superparamagnetic nanoparticles with uniaxial anisotropy. J Appl Phys 107(12):123909

89. Landi GT, Bakuzis AF (2012) On the energy conversion efficiency in magnetic hyperthermia applications: a new perspective to analyze the departure from the linear regime. J Appl Phys 111(8):083915

90. Hergt R, Hiergeist R, Zeisberger M, Schüler D, Heyen U, Hilger I, Kaiser WA (2005) Magnetic properties of bacterial magnetosomes as potential diagnostic and therapeutic tools. J Magn Magn Mater 293(1):80–86

91. Lartigue L, Innocenti C, Kalaivani T, Awwad A, Sanchez Duque MDM, Guari Y, Larionova J, Guérin C, Montero J-LG, Barragan-Montero V, Arosio P, Lascialfari A, Gatteschi D, Sangregorio C (2011) Water-dispersible sugar-coated iron oxide nanoparticles An evaluation of their relaxometric and magnetic hyperthermia properties. J Am Chem Soc 133 (27):10459–10472

92. Levy M, Quarta A, Espinosa A, Figuerola A, Wilhelm C, García-Hernández M, Genovese A, Falqui A, Alloyeau D, Buonsanti R, Cozzoli PD, García MA, Gazeau F, Pellegrino T (2011) Correlating magneto-structural properties to hyperthermia performance of highly monodisperse iron oxide nanoparticles prepared by a seeded-growth route. Chem Mater 23 (18):4170–4180

93. Bakoglidis KD, Simeonidis K, Sakellari D, Stefanou G, Angelakeris M (2012) Size-dependent mechanisms in ac magnetic hyperthermia response of iron-oxide nanoparticles. IEEE Trans Magn 48(4):1320–1323

94. Hugounenq P, Levy M, Alloyeau D, Lartigue L, Dubois E, Cabuil V, Ricolleau C, Roux S, Wilhelm C, Gazeau F, Bazzi R (2012) Iron oxide monocrystalline nanoflowers for highly efficient magnetic hyperthermia. J Phys Chem C 116(29):15702–15712

95. Khandhar AP, Ferguson RM, Simon JA, Krishnan KM (2012) Tailored magnetic nanoparticles for optimizing magnetic fluid hyperthermia. J Biomed Mater Res A 100A(3):728–737

96. de la Presa P, Luengo Y, Multigner M, Costo R, Morales MP, Rivero G, Hernando A (2012) Study of heating efficiency as a function of concentration, size, and applied field in γ-Fe_2O_3 nanoparticles. J Phys Chem C 116(48):25602–25610

97. Chen S-W, Chiang C-L, Chen C-L (2012) The influence of nanoparticle size and external AC magnetic field on heating ability. Mater Lett 67(1):349–351

98. Lima EJ, De Biasi E, Vasquez Mansilla M, Saleta ME, Granada M, Troiani HE, Effenberger FB, Rossi LM, Rechenberg HR, Zysler RD (2013) Heat generation in agglomerated ferrite nanoparticles in an alternating magnetic field. J Phys D Appl Phys 46(4):045002

99. Chen R, Christiansen MG, Anikeeva P (2013) Maximizing hysteretic losses in magnetic ferrite nanoparticles via model-driven synthesis and materials optimization. ACS Nano 7 (10):8990–9000

100. Mehdaoui B, Meffre A, Lacroix L-M, Carrey J, Lachaize S, Respaud M, Gougeon M, Chaudret B (2010) Magnetic anisotropy determination and magnetic hyperthermia properties of small Fe nanoparticles in the superparamagnetic regime. J Appl Phys 107(9):09A324

101. Ichiyanagi Y, Shigeoka D, Hiroki T, Mashino T, Kimura S, Tomitaka A, Ueda K, Takemura Y (2012) Study on increase in temperature of Co–Ti ferrite nanoparticles for magnetic hyperthermia treatment. Thermochim Acta 532:123–126

102. Józefczak A, Hornowski T, Skumiel A, Łabowski M, Timko M, Kopčanský P, Koneracká M, Szlaferek A, Kowalski W (2009) Effect of poly (ethylene glycol) coating on the magnetic and thermal properties of biocompatible magnetic liquids. J Magn Magn Mater 321 (10):1505–1508

103. Gonzales-Weimuller M, Zeisberger M, Krishnan KM (2009) Size-dependant heating rates of iron oxide nanoparticles for magnetic fluid hyperthermia. J Magn Magn Mater 321 (13):1947–1950

104. Skumiel A, Hornowski T, Józefczak A (2011) Heating characteristics of transformer oil-based magnetic fluids of different magnetic particle concentrations. Int J Thermophys 32(4):876–885

105. Barick KC, Hassan PA (2012) Glycine passivated Fe_3O_4 nanoparticles for thermal therapy. J Colloid Interface Sci 369(1):96–102

106. Guardia P, Di Corato R, Lartigue L, Wilhelm C, Espinosa A, Garcia-Hernandez M, Gazeau F, Manna L, Pellegrino T (2012) Water-soluble iron oxide nanocubes with high values of specific absorption rate for cancer cell hyperthermia treatment. ACS Nano 6(4):3080–3091

107. Diamantopoulos G, Basina G, Tzitzios V, Karakosta E, Fardis M, Jaglicic Z, Lazaridis N, Papavassiliou G (2013) Magnetic hyperthermia of laponite based ferrofluid. J Magn Magn Mater 336:71–74

108. Gkanas EI (2013) In vitro magnetic hyperthermia response of iron oxide MNP's incorporated in DA3, MCF-7 and HeLa cancer cell lines. Cent Eur J Chem 11(7):1042–1054

109. Sadat ME, Patel R, Sookoor J, Bud'ko SL, Ewing RC, Zhang J, Xu H, Wang Y, Pauletti GM, Mast DB, Shi D (2014) Effect of spatial confinement on magnetic hyperthermia via dipolar interactions in Fe_3O_4 nanoparticles for biomedical applications. Mater Sci Eng C 42:52–63

110. Dong-Hyun K, Thai YT, Nikles DE, Brazel CS (2009) Heating of aqueous dispersions containing $MnFe_2O_3$ nanoparticles by radio-frequency magnetic field induction. IEEE Trans Magn 45(1):64–70

111. Ibrahim EMM, Hampel S, Wolter AUB, Kath M, El-Gendy AA, Klingeler R, Täschner C, Khavrus VO, Gemming T, Leonhardt A, Büchner B (2012) Superparamagnetic FeCo and FeNi nanocomposites dispersed in submicrometer-sized C spheres. J Phys Chem C 116 (42):22509–22517

112. Tannous C, Gieraltowski J (2008) The Stoner–Wohlfarth model of ferromagnetism. Eur J Phys 29(3):475

113. Stoner EC, Wohlfarth EP (1948) A mechanism of magnetic hysteresis in heterogeneous alloys. Philos Trans R Soc Lond A Math Phys Sci 240(826):599–642

114. García-Otero J, García-Bastida AJ, Rivas J (1998) Influence of temperature on the coercive field of non-interacting fine magnetic particles. J Magn Magn Mater 189(3):377–383

115. Hergt R, Andra W, d'Ambly CG, Hilger I, Kaiser WA, Richter U, Schmidt HG (1998) Physical limits of hyperthermia using magnetite fine particles. IEEE Trans Magn 34(5):3745–3754

116. Lu JJ, Huei Li H, Klik I (1994) Field orientations and sweep rate effects on magnetic switching of Stoner-Wohlfarth particles. J Appl Phys 76(3):1726–1732

117. Verde EL, Landi GT, Carrião MS, Drummond AL, Gomes JA, Vieira ED, Sousa MH, Bakuzis AF (2012) Field dependent transition to the non-linear regime in magnetic hyperthermia experiments: comparison between maghemite, copper, zinc, nickel and cobalt ferrite nanoparticles of similar sizes. AIP Adv 2(3):032120

118. Usov NA, Grebenshchikov YB (2009) Hysteresis loops of an assembly of superparamagnetic nanoparticles with uniaxial anisotropy. J Appl Phys 106(2):11

119. Lacroix L-M, Malaki RB, Carrey J, Lachaize S, Respaud M, Goya GF, Chaudret B (2009) Magnetic hyperthermia in single-domain monodisperse FeCo nanoparticles: evidences for Stoner–Wohlfarth behavior and large losses. J Appl Phys 105(2):023911

120. Bae S, Sang Won L, Hirukawa A, Takemura Y, Youn Haeng J, Sang Geun L (2009) AC magnetic-field-induced heating and physical properties of ferrite nanoparticles for a hyperthermia agent in medicine. IEEE Trans Nano 8(1):86–94

121. Timko M, Dzarova A, Kovac J, Skumiel A, Józefczak A, Hornowski T, Gojżewski H, Zavisova V, Koneracka M, Sprincova A, Strbak O, Kopcansky P, Tomasovicova N (2009) Magnetic properties and heating effect in bacterial magnetic nanoparticles. J Magn Magn Mater 321(10):1521–1524

122. Müller R, Dutz S, Habisreuther T, Zeisberger M (2011) Investigations on magnetic particles prepared by cyclic growth. J Magn Magn Mater 323(10):1223–1227

123. Alphandéry E, Guyot F, Chebbi I (2012) Preparation of chains of magnetosomes, isolated from Magnetospirillum magneticum strain AMB-1 magnetotactic bacteria, yielding efficient treatment of tumors using magnetic hyperthermia. Int J Pharm 434(1–2):444–452

124. Chen X, Klingeler R, Kath M, El Gendy AA, Cendrowski K, Kalenczuk RJ, Borowiak-Palen E (2012) Magnetic silica nanotubes: synthesis, drug release, and feasibility for magnetic hyperthermia. ACS Appl Mater Interfaces 4(4):2303–2309

125. Sotiriou GA, Visbal-Onufrak MA, Teleki A, Juan EJ, Hirt AM, Pratsinis SE, Rinaldi C (2013) Thermal energy dissipation by SiO_2-coated plasmonic-superparamagnetic nanoparticles in alternating magnetic fields. Chem Mater 25(22):4603–4612

126. Filippousi M, Altantzis T, Stefanou G, Betsiou M, Bikiaris DN, Angelakeris M, Pavlidou E, Zamboulis D, Van Tendeloo G (2013) Polyhedral iron oxide core-shell nanoparticles in a biodegradable polymeric matrix: preparation, characterization and application in magnetic particle hyperthermia and drug delivery. RSC Adv 3(46):24367–24377

127. Mehdaoui B, Meffre A, Lacroix LM, Carrey J, Lachaize S, Gougeon M, Respaud M, Chaudret B (2010) Large specific absorption rates in the magnetic hyperthermia properties of metallic iron nanocubes. J Magn Magn Mater 322(19):L49–L52

128. Serantes D, Baldomir D, Martinez-Boubeta C, Simeonidis K, Angelakeris M, Natividad E, Castro M, Mediano A, Chen D-X, Sanchez A, Balcells L, Martínez B (2010) Influence of dipolar interactions on hyperthermia properties of ferromagnetic particles. J Appl Phys 108 (7):073918

129. El-Gendy AA, Ibrahim EMM, Khavrus VO, Krupskaya Y, Hampel S, Leonhardt A, Büchner B, Klingeler R (2009) The synthesis of carbon coated Fe, Co and Ni nanoparticles and an examination of their magnetic properties. Carbon 47(12):2821–2828

130. Pollert E, Veverka P, Veverka M, Kaman O, Závěta K, Vasseur S, Epherre R, Goglio G, Duguet E (2009) Search of new core materials for magnetic fluid hyperthermia: preliminary chemical and physical issues. Prog Solid State Chem 37(1):1–14

131. Mehdaoui B, Carrey J, Stadler M, Cornejo A, Nayral C, Delpech F, Chaudret B, Respaud M (2012) Influence of a transverse static magnetic field on the magnetic hyperthermia properties and high-frequency hysteresis loops of ferromagnetic FeCo nanoparticles. Appl Phys Lett 100 (5):052403

132. Mehdaoui B, Tan RP, Meffre A, Carrey J, Lachaize S, Chaudret B, Respaud M (2013) Increase of magnetic hyperthermia efficiency due to dipolar interactions in low-anisotropy magnetic nanoparticles: theoretical and experimental results. Phys Rev B 87(17):174419

133. Yang Y, Liu X, Yang Y, Xiao W, Li Z, Xue D, Li F, Ding J (2013) Synthesis of nonstoichiometric zinc ferrite nanoparticles with extraordinary room temperature magnetism and their diverse applications. J Mater Chem C 1(16):2875–2885

134. Zélis PM, Pasquevich GA, Stewart SJ, van Raap MBF, Aphesteguy J, Bruvera IJ, Laborde C, Pianciola B, Jacobo S, Sánchez FH (2013) Structural and magnetic study of zinc-doped magnetite nanoparticles and ferrofluids for hyperthermia applications. J Phys D Appl Phys 46(12):125006

135. Atkinson WJ, Brezovich IA, Chakraborty DP (1984) Usable frequencies in hyperthermia with thermal seeds. IEEE Trans Biomed Eng BME-31(1):70–75

136. Johannsen M, Gneveckow U, Thiesen B, Taymoorian K, Cho CH, Waldöfner N, Scholz R, Jordan A, Loening SA, Wust P (2007) Thermotherapy of prostate cancer using magnetic nanoparticles: feasibility, imaging, and three-dimensional temperature distribution. Eur Urol 52(6):1653–1662

137. Maier-Hauff K, Rothe R, Scholz R, Gneveckow U, Wust P, Thiesen B, Feussner A, Deimling A, Waldoefner N, Felix R, Jordan A (2007) Intracranial thermotherapy using magnetic nanoparticles combined with external beam radiotherapy: results of a feasibility study on patients with glioblastoma multiforme. J Neurooncol 81(1):53–60

138. Bekovic M, Ban I, Hamler A (2010) Assessment of magnetic fluid losses out of magnetic properties measurement. J Phys Conf Ser 200(7):072010

139. Natividad E, Castro M, Mediano A (2011) Adiabatic magnetothermia makes possible the study of the temperature dependence of the heat dissipated by magnetic nanoparticles under alternating magnetic fields. Appl Phys Lett 98(24):243119

140. Natividad E, Castro M, Goglio G, Andreu I, Epherre R, Duguet E, Mediano A (2012) New insights into the heating mechanisms and self-regulating abilities of manganite perovskite nanoparticles suitable for magnetic fluid hyperthermia. Nanoscale 4(13):3954–3962

141. Ondeck CL, Habib AH, Ohodnicki P, Miller K, Sawyer CA, Chaudhary P, McHenry ME (2009) Theory of magnetic fluid heating with an alternating magnetic field with temperature dependent materials properties for self-regulated heating. J Appl Phys 105(7):07B324

142. Bertoni G, Torre B, Falqui A, Fragouli D, Athanassiou A, Cingolani R (2011) Nanochains formation of superparamagnetic nanoparticles. J Phys Chem C 115(15):7249–7254
143. Andreu I, Natividad E, Solozábal L, Roubeau O (2015) Same magnetic nanoparticles, different heating behavior: influence of the arrangement and dispersive medium. J Magn Magn Mater 380:341–346
144. Chamberlin RV, Hemberger J, Loidl A, Humfeld KD, Farrell D, Yamamuro S, Ijiri Y, Majetich SA (2002) Percolation, relaxation halt, and retarded van der Waals interaction in dilute systems of iron nanoparticles. Phys Rev B 66(17):172403
145. Fortin J-P, Gazeau F, Wilhelm C (2008) Intracellular heating of living cells through Néel relaxation of magnetic nanoparticles. Eur Biophys J 37(2):223–228
146. Dormann JL, Bessais L, Fiorani D (1988) A dynamic study of small interacting particles: superparamagnetic model and spin-glass laws. J Phys C 21(10):2015
147. Dormann JL, Fiorani D, Tronc E (1999) On the models for interparticle interactions in nanoparticle assemblies: comparison with experimental results. J Magn Magn Mater 202 (1):251–267
148. Mørup S, Tronc E (1994) Superparamagnetic relaxation of weakly interacting particles. Phys Rev Lett 72(20):3278–3281
149. Hansen MF, Mørup S (1998) Models for the dynamics of interacting magnetic nanoparticles. J Magn Magn Mater 184(3):L262–L274
150. Déjardin P-M (2011) Magnetic relaxation of a system of superparamagnetic particles weakly coupled by dipole-dipole interactions. J Appl Phys 110(11):113921
151. Shtrikman S, Wohlfarth EP (1981) The theory of the Vogel-Fulcher law of spin glasses. Phys Lett A 85(8–9):467–470
152. Landi GT (2013) The random dipolar-field approximation for systems of interacting magnetic particles. J Appl Phys 113(16):163908
153. Landi GT (2014) Role of dipolar interaction in magnetic hyperthermia. Phys Rev B 89 (1):014403
154. Urtizberea A, Natividad E, Arizaga A, Castro M, Mediano A (2010) Specific absorption rates and magnetic properties of ferrofluids with interaction effects at low concentrations. J Phys Chem C 114(11):4916–4922
155. Branquinho LC, Carrião MS, Costa AS, Zufelato N, Sousa MH, Miotto R, Ivkov R, Bakuzis AF (2013) Effect of magnetic dipolar interactions on nanoparticle heating efficiency: implications for cancer hyperthermia. Sci Rep 3:2887
156. Serantes D, Simeonidis K, Angelakeris M, Chubykalo-Fesenko O, Marciello M, Morales MdP, Baldomir D, Martinez-Boubeta C (2014) Multiplying magnetic hyperthermia response by nanoparticle assembling. J Phys Chem C 118(11):5927–5934
157. Tan RP, Carrey J, Respaud M (2014) Magnetic hyperthermia properties of nanoparticles inside lysosomes using kinetic Monte Carlo simulations: influence of key parameters and dipolar interactions, and evidence for strong spatial variation of heating power. Phys Rev B 90 (21):214421
158. Haase C, Nowak U (2012) Role of dipole-dipole interactions for hyperthermia heating of magnetic nanoparticle ensembles. Phys Rev B 85(4):045435
159. Andreu I, Natividad E, Solozábal L, Roubeau O (2015) Nano-objects for addressing the control of nanoparticle arrangement and performance in magnetic hyperthermia. ACS Nano 9(2):1408–1419